
Masters Theses

Student Theses and Dissertations

Fall 2016

Material properties characterization for multilayer PCB and PEEC macromodels for above plane decoupling capacitors

Xiang Fang

Follow this and additional works at: https://scholarsmine.mst.edu/masters_theses



Part of the [Electrical and Computer Engineering Commons](#)

Department:

Recommended Citation

Fang, Xiang, "Material properties characterization for multilayer PCB and PEEC macromodels for above plane decoupling capacitors" (2016). *Masters Theses*. 7943.

https://scholarsmine.mst.edu/masters_theses/7943

This thesis is brought to you by Scholars' Mine, a service of the Missouri S&T Library and Learning Resources. This work is protected by U. S. Copyright Law. Unauthorized use including reproduction for redistribution requires the permission of the copyright holder. For more information, please contact scholarsmine@mst.edu.

MATERIAL PROPERTIES CHARACTERIZATION FOR MULTILAYER PCB AND
PEEC MACROMODELS FOR ABOVE PLANE
DECOUPLING CAPACITORS

by

XIANG FANG

A THESIS

Presented to the Faculty of the Graduate School of the
MISSOURI UNIVERSITY OF SCIENCE AND TECHNOLOGY

In Partial Fulfillment of the Requirements for the Degree

MASTER OF SCIENCE IN ELECTRIC ENGINEERING

2016

Approved by

Dr. Jun Fan, Advisor
Dr. James L. Drewniak
Dr. Mikheil Tsiklauri

© 2016

XIANG FANG

All Rights Reserved

ABSTRACT

Accurate frequency-dependent dielectric properties are important for accurate modelling of signal and power integrity problems. And decoupling capacitors perform an important function in the impedance reduction of power distribution systems. Hence, precise dielectric properties and micromodels for decoupling capacitors are the key parts for the signal and power integrity design.

In Section 1, the existing method for extracting dielectric properties from fabricated multilayer printed circuit boards based on the measured electrical property of fabricated transmission lines is introduced and validated using simulations. And the potential errors in the procedure are discussed. After that Djordjevic-Sarkar causal dielectric model for dielectric properties is studied and a new extraction method is proposed which takes advantage of differential and common mode behavior of differential stripline to remove the roughness effect and extract the transmission line based dielectric constant (DK) and dissipation factor (DF).

In Section 2, circuit macromodels are constructed for the decoupling capacitors, which include the local environment, such that the overall power distribution network (PDN) model is simplified. Such a macromodel must be sufficiently decoupled from the rest of the PDN system such that the coupling can be ignored with a sufficiently small error. The macromodel for the capacitance environment will simplify the modeling of the rest of the PDN system.

ACKNOWLEDGMENTS

Foremost, I would like to express my sincere gratitude to my advisor, Dr. Jun Fan, for his patience, motivation, enthusiasm, and immense knowledge through my Master degree study and research. He taught me to be motivated and focus on the research work and also gave me great suggestions for the career development. I could not have imagined having a better advisor and mentor for my three years' graduate study.

I would also like to thank Dr. Drewniak, who brought me into EMC Lab and taught me his great research experience. Thanks very much for his trust on me and giving me an intern chance in DELL to release my financial burden for my family. I would like to thank Dr. Mikheil Tsiklauri for giving mathematical support during my research and he is really the smartest I have ever seen. I would like to thank Dr. David Pommerenke , Dr. Beetner and Dr. Victor Khilkevich for their advice and help on my research work.

I thank my fellow lab mates in the EMC group of Missouri S&T: Qiaolei Huang, Liang Li, Guangyao Sheng, Yansheng Wang and Jiayi He for the help in my research and life in Rolla. And thanks Hui Gao to share one happy year with me.

Finally, I would like to thank my family: my mother Liuxi You and father Qinghua Fang, for giving birth to me at the first place and supporting me spiritually throughout my life. I dedicate this thesis to both of them.

This thesis is based upon work supported partially by the National Science Foundation under Grant No. IIP-1440110.

TABLE OF CONTENTS

| | Page |
|---|------|
| ABSTRACT..... | iii |
| ACKNOWLEDGMENTS | iv |
| LIST OF ILLUSTRATIONS..... | vii |
| SECTION | |
| 1. INTRODUCTION..... | 1 |
| 2. MATERIAL PROPERTIES CHARACTERIZATION FOR MULILAYER PCB ... | 4 |
| 2.1. METHODOLOGY OF MATERIAL CHARACTERIZATION | 4 |
| 2.1.1. Material Characterization from Smooth Conductor..... | 5 |
| 2.1.2. Material Characterization from Rough Conductor..... | 6 |
| 2.2. EXTRACTION METHOD VALIDATION BY SIMULATIONS | 9 |
| 2.2.1. Simulaiton Validation for Smooth Conductor..... | 9 |
| 2.2.2. Simulaiton Validation for Rough Conductor.. | 12 |
| 2.3. SENSITIVITY ANALYSIS FOR 'ROOT MEAN' METHOD | 14 |
| 2.4. INNOVATIVE MATERIAL MODEL DERIVATIONS..... | 15 |
| 2.4.1. Separation of Conductor and Dielectric Contributions. | 15 |
| 2.4.2. Djordjevic-Sarkar Casual Dielectric Model | 18 |
| 2.4.3. Huray Model for Surface Roughness. | 20 |
| 2.4.4. DK and DF Extraction by Differential and Common Mode..... | 21 |
| 2.5. MEASUREMENT AND RESULTS COMPARISON..... | 23 |
| 2.5.1. Test Board Geometries..... | 23 |
| 2.5.2. Measurement Set Up | 25 |

| | |
|--|----|
| 2.5.3. Extracion Results Comapred with Measurement Data..... | 26 |
| 2.5.3.1 DK and DF extraction from intel VLP board measurement..... | 26 |
| 2.5.3.2 DK and DF extraction from cisco VLP2 board measurement..... | 29 |
| 2.5.3.3 DK and DF extraction from cisco PCIe board measurement | 31 |
| 3. PEEC MACROMODELS FOR ABOVE PLANE DECOUPLING CAPACITRORS | 33 |
| 3.1. MODELING OF L-ABOVE | 33 |
| 3.2. PEEC MODELS FOR DISTRIBUTED AND LUMPDED MODELS | 35 |
| 3.3. NUMERICAL AND TEST RESULTS | 38 |
| 4. CONCLUSIONS..... | 43 |
| BIBLIOGRAPHY..... | 44 |
| VITA | 46 |

LIST OF ILLUSTRATIONS

| | Page |
|---|------|
| Figure 2.1. Flowchart of the “Root-omega” method | 4 |
| Figure 2.2. Illustration of the cross-section of a rough stripline | 8 |
| Figure 2.3. Cross section of the narrow trace | 9 |
| Figure 2.4. Cross section of the wide trace..... | 9 |
| Figure 2.5. Validating simulation results..... | 10 |
| Figure 2.6. DK and DF extraction for a large DF material..... | 10 |
| Figure 2.7. DK and DF extraction for a small DF material | 11 |
| Figure 2.8. Cross section of the rough narrow trace | 12 |
| Figure 2.9. Cross section of the rough wide trace..... | 13 |
| Figure 2.10. DK and DF extraction for a large DF material from two rough traces | 13 |
| Figure 2.11. DK and DF extraction for a small DF material from two rough traces..... | 14 |
| Figure 2.12. Separate α_T into conductor part and dielectric part..... | 17 |
| Figure 2.13. Separate β_T into conductor part and dielectric part..... | 17 |
| Figure 2.14. Flow chart of DK and DF extraction by differential and common mode parameters | 21 |
| Figure 2.15. Intel’s VLP test board..... | 23 |
| Figure 2.16. Cross-section of the VLP test board..... | 24 |
| Figure 2.17. Cisco’s VLP2 test board..... | 24 |
| Figure 2.18. Cross-section of the VLP2 test board..... | 24 |
| Figure 2.19. Cisco’s PCIe test board | 25 |
| Figure 2.20. Cross-section of the PCIe test board | 25 |
| Figure 2.21. Four-port PNA with frequency band up to 50GHz | 25 |
| Figure 2.22. Material characterization flow chart..... | 26 |

| | |
|---|----|
| Figure 2.23. Intel VLP board extraction results..... | 26 |
| Figure 2.24. Sdd21 magnitude comparison of Intel board..... | 27 |
| Figure 2.25. Sdd21 phase comparison of Intel board | 27 |
| Figure 2.26. Scc21 magnitude comparison of Intel board | 28 |
| Figure 2.27. Scc21 phase comparison of Intel board..... | 28 |
| Figure 2.28. Cisco VLP2 board extraction results..... | 29 |
| Figure 2.29. Sdd21 magnitude comparison of Cisco VLP2 board | 29 |
| Figure 2.30. Sdd21 phase comparison of Cisco VLP2 board | 30 |
| Figure 2.31. Scc21 magnitude comparison of Cisco VLP2 board..... | 30 |
| Figure 2.32. Scc21 phase comparison of Cisco VLP2 board | 30 |
| Figure 2.33. Cisco PCIe board extraction results | 31 |
| Figure 2.34. Sdd21 magnitude comparison of Cisco PCIe board..... | 31 |
| Figure 2.35. Sdd21 phase comparison of Cisco PCIe board..... | 31 |
| Figure 2.36. Scc21 magnitude comparison of Cisco PCIe board.. | 32 |
| Figure 2.37. Scc21 phase comparison of Cisco PCIe board | 32 |
| Figure 3.1. Decoupling capacitor's mounting environment | 33 |
| Figure 3.2. Simplified three-layer model for decoupling capacitors. | 34 |
| Figure 3.3. Top view of connections to the capacitor with ground plane underneath | 34 |
| Figure 3.4. Side view of simplified cross-section model for (a) Simple layer of combined lumped capacitor and distributed PEEC model (b) | 38 |
| Figure 3.5. Response as a function of the number of C_d capacitances (a) Distribution of the lumped capacitance (b)..... | 36 |
| Figure 3.6. Approximate inductance of the model for different ground plane | 39 |
| Figure 3.7. Table of macromodel inductances of different ground plane distance..... | 39 |
| Figure 3.8. Single pole Debye model for lossy dielectric | 40 |
| Figure 3.9. Comparison of mode with and without loss | 40 |

| | |
|--|----|
| Figure 3.10. Macromodel which includes parallel resonance and loss dielectric..... | 41 |
| Figure 3.11. Impedance curve comparison for PEEC and macromodel..... | 41 |
| Figure 3.12. Table of equivalent circuit value for different ground spacing | 42 |

1. INTRODUCTION

Dielectric material plays an important role in signal integrity (SI) and power integrity (PI) [1][2][3][4]. For example, when designing channels in high-speed products, the geometry and dielectric material properties determine the electrical performance, such as the network parameters, eye diagram, radiation patterns, and so on. Design optimizations are often carried out and material choice is usually made as a trade-off between electrical performance and cost [5][6][7]. If the material properties are not correct or not accurate enough, the design could either fail to meet the performance specifications resulting in a costly re-spin, or become over-designed by using a more costly, higher performance board material.

Material vendors usually provide the material properties measured in the narrow bandwidth by the coaxial probing method, the resonant cavity method, and the waveguide or antenna wave propagation method. However, this information is obtained before board fabrication. It provides references but usually is not accurate enough for high-speed design.

When multiple dielectric layers are fabricated together to form a multilayer printed circuit board (PCB), the effective dielectric properties after fabrication will change due to treatments and reflow of the prepreg layers. So extracting material properties after fabrication is more meaningful for board designers. PCB resonant cavities can be constructed using parallel planes and shorting vias in a fabricated multilayer PCB; however, the DK and DF extraction from a cavity is inherently a narrow band method since the accuracy is only good at the resonances. The transmission line based method can provide a wide band response. In this paper, an implementation of the transmission-

line based method denoted the “Root-omega” method is studied [2][3][4][8][9]. Potential errors in the procedure are also discussed.

The “Root-omega” method is based on the measured S-parameters of fabricated striplines in a multilayer PCB. The effects of the test fixtures need to be eliminated by calibration or de-embedding to ensure the accuracy. When the conductor surface is smooth, only one stripline is needed. The method can separate the conductor and dielectric losses based on their frequency-dependent behaviors [10][11].

When the conductor surface is rough, the effect of surface roughness needs to be further removed before DK and DF can be accurately extracted. The “Root-omega” method can be extended [2]. However, two striplines with different trace widths are necessary. These two traces are assumed to have the same dielectric properties. The total attenuation factor (α_T) and propagation constant (β_T) of the traces are separated into smooth conductor contributions, rough conductor contributions and dielectric contributions. The extracted dielectric attenuation factor (α_D) and propagation constant (β_D) are used for the final material property extraction.

After that Djordjevic-Sarkar causal dielectric model for dielectric properties are studied and a new extraction method is proposed which takes advantage of differential and common mode behavior of differential stripline to remove the roughness effect and extract the transmission line based dielectric constant (DK) and dissipation factor (DF).

Decoupling capacitors perform an important function in the impedance reduction of power distribution systems. Integrated circuits of all types need low impedance voltage supplies. Decoupling capacitors perform an important function in the impedance reduction of Power Distribution Network (PDN) systems. Hence, they are a key part of

an electrical model required for the design of such systems. The circuit models provided by the manufacturers of the component usually consists of an inductor (ESL), a resistor (ESR) and a capacitance (ESC). We show that this data is insufficient for obtaining useful simple models.

The key problem is that the above plane decoupling capacitors are strongly coupled to the local environment. Hence, it is impossible to represent the capacitors without the knowledge of the details of the environment, e.g., the spacing to the planes as well as the connection wires. The important issue is to find connections which allow a system to be subdivided into parts which are sufficiently decoupled. This is an on-going area of research [12].

Circuit macromodels for the decoupling capacitors are constructed, which include the local environment, such that the overall PDN model is simplified. Such a macromodel must be sufficiently decoupled from the rest of the PDN system such that the coupling can be ignored with a sufficiently small error. The macromodel for the capacitance environment will simplify the modeling of the rest of the PDN system. Simple PEEC models of the local couplings have been considered before [13]. This work represents a more detailed model which also considers partitioning aspects.

2. MATERIAL PROPERTIES CHARACTERIZATION FOR MULTILAYER PCB

2.1. METHODOLOGY OF MATERIAL CHARACTERIZATION

The flowchart of the ‘‘Root-omega’’ method is shown in Figure 2.1. The method is based on the S-parameters of the fabricated trace in a PCB. The S-parameters are converted to the ABCD parameters, and the complex propagation constant is calculated as [2][3]

$$\gamma = \frac{\operatorname{arccosh}(\sqrt{A \cdot D})}{\text{linelength}}; \text{ and } \gamma = \alpha_T + j\beta_T \quad (2.1)$$

$$\text{Where } \begin{bmatrix} A & B \\ C & D \end{bmatrix} = \begin{bmatrix} \cosh \gamma l & Z_0 \sinh \gamma l \\ \frac{1}{Z_0 \sinh \gamma l} & \cosh \gamma l \end{bmatrix}, \alpha_T \text{ and } \beta_T \text{ are the total attenuation}$$

factor and the total propagation constant.

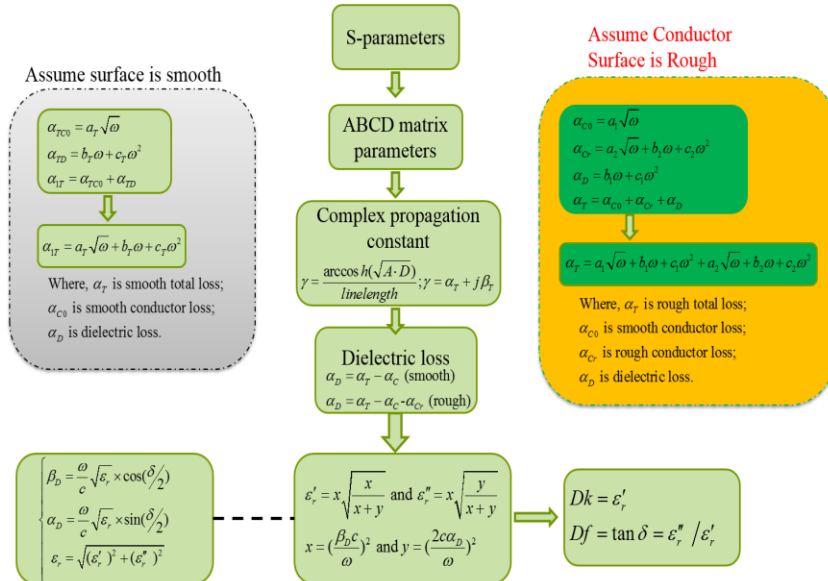


Figure 2.1. Flowchart of the ‘‘Root-omega’’ method

After the total attenuation factor and propagation constant are obtained, they are used to extract the dielectric contributions. The equivalent DK and DF values of the dielectric media where the traces are placed in are calculated from the dielectric attenuation factor α_D and the dielectric propagation constant β_D as

$$\begin{aligned} DK &= \varepsilon'_r = x \sqrt{\frac{x}{x+y}} \\ DF &= \frac{\varepsilon''_r}{\varepsilon'_r} = \sqrt{\frac{y}{x}} \end{aligned} \quad (2.2)$$

Where $x = \left(\frac{\beta_D c}{\omega}\right)^2$, and $y = \left(\frac{2c\alpha_D}{\omega}\right)^2$. The c and ω are the free-space velocity and the angular frequency, respectively.

2.1.1. Material Characterization from Smooth Conductor. When the conductor surface is assumed to be smooth, the total attenuation factor and propagation constant can be separated into two portions. Take the total attenuation constant α_T as an example. It can be fitted as

$$\alpha_T = a\sqrt{\omega} + b\omega + c\omega^2 \quad (2.3)$$

Since the conductor loss α_C due to the skin effect is proportional to the square root of frequency and the dielectric loss α_D is proportional to frequency and the square of frequency, we have

$$\alpha_C = a\sqrt{\omega} \quad (2.4)$$

$$\alpha_D = b\omega + c\omega^2 \quad (2.5)$$

In other words, curve fitting function is used to separate the dielectric loss from the conductor loss. When α_D and β_D are obtained, DK and DF can be calculated by (2.2).

2.1.2. Material Characterization from Rough Conductor. When the conductor surface is rough, the total attenuator factor and propagation constant have the smooth conductor, rough conductor, and dielectric contributions. Let's again take the total attenuation factor as an example. Assuming the additional rough conductor contribution is $\alpha_{Cr} = a_2\sqrt{\omega} + b_2\omega + c_2\omega^2$, the total attenuation factor can be written as

$$\begin{aligned}\alpha_T &= \alpha_{C0} + \alpha_D + \alpha_{Cr} \\ &= \boxed{a_1\sqrt{\omega}} + \boxed{b_1\omega + c_1\omega^2} + \boxed{a_2\sqrt{\omega} + b_2\omega + c_2\omega^2} \\ &= (a_1 + a_2)\sqrt{\omega} + (b_1 + b_2)\omega + (c_1 + c_2)\omega^2\end{aligned}\quad (2.6)$$

Where a_1 is the coefficient for α_C ; b_1, c_1 are coefficients for α_D and a_2, b_2, c_2 are coefficients for α_{Cr} .

Since the rough conductor contribution has similar frequency-dependency, it needs two striplines with different widths to further distinguish the additional term. These two narrow and wide traces, need to have the same dielectric contributions, which means b_1^N and c_1^N are equal to b_1^W and c_1^W , respectively, in the following expressions where the total attenuation factors for the narrow and wide traces are curve fitted into the three terms individually.

$$\begin{aligned}\alpha_T^N &= K_1^N\sqrt{\omega} + K_2^N\omega + K_3^N\omega^2 \\ &= (a_1^N + a_2^N)\sqrt{\omega} + (b_1^N + b_2^N)\omega + (c_1^N + c_2^N)\omega^2\end{aligned}\quad (2.7)$$

$$\begin{aligned}\alpha_T^W &= K_1^W\sqrt{\omega} + K_2^W\omega + K_3^W\omega^2 \\ &= (a_1^W + a_2^W)\sqrt{\omega} + (b_1^W + b_2^W)\omega + (c_1^W + c_2^W)\omega^2\end{aligned}\quad (2.8)$$

Where $K_1 = a_1 + a_2$, $K_2 = b_1 + b_2$ and $K_3 = c_1 + c_2$. K_1, K_2 and K_3 are the coefficients of the three terms in the total attenuation factor. The superscript 'N' means

the narrow trace and the superscript ‘W’ means the wide trace. From (2.7) and (2.8), we have further obtain

$$\begin{cases} K_1^N - K_1^W = a_1^N \left(1 - \frac{a_1^W}{a_1^N} \right) + a_2^N \left(1 - \frac{a_2^W}{a_2^N} \right) \\ K_1^N + K_1^W = a_1^N \left(1 + \frac{a_1^W}{a_1^N} \right) + a_2^N \left(1 + \frac{a_2^W}{a_2^N} \right) \\ K_2^N - K_2^W = b_2^N \left(1 - \frac{b_2^W}{b_2^N} \right) \\ K_3^N - K_3^W = c_2^N \left(1 - \frac{c_2^W}{c_2^N} \right) \end{cases} \quad (2.9)$$

Material Characterization from Rough conductor and the roughness information are further known (which can be obtained from an SEM measurement if needed by cutting the board and treating the cross section), the coefficient ratios can be estimated based on the physical understanding of the loss mechanisms as

$$\begin{cases} \frac{a_1^W}{a_1^N} = \frac{P^N}{P^W} \\ \frac{a_2^W}{a_2^N} = \frac{(A_1^W/w_1^W + A_2^W/w_2^W) \times t^N}{(A_1^N/w_1^N + A_2^N/w_2^N) \times t^W} \\ \frac{b_2^W}{b_2^N} = \frac{P^N}{P^W} \times \frac{(A_1^W/\Lambda_1^W + A_2^W/\Lambda_2^W)}{(A_1^N/\Lambda_1^N + A_2^N/\Lambda_2^N)} \\ \frac{c_2^W}{c_2^N} = \frac{P^N}{P^W} \times \frac{(A_1^W/\Lambda_1^W + A_2^W/\Lambda_2^W)}{(A_1^N/\Lambda_1^N + A_2^N/\Lambda_2^N)} \end{cases} \quad (2.10)$$

Where, as illustrated in Figure 2.2, P is the perimeter of the trace cross-section; A is the peak to valley amplitude of the roughness; Λ is the peak-to-peak roughness period; t is the trace thickness; and, w is the trace width. The subscript ‘1’ is for the oxide side and ‘2’ is for the foil side of the trace.

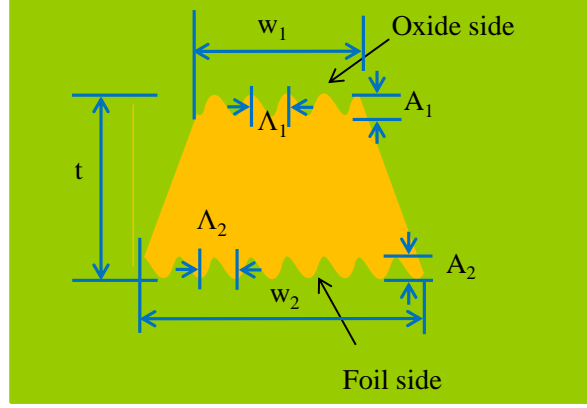


Figure 2.2. Illustration of the cross-section of a rough stripline

After removing the surface roughness effect, the dielectric attenuation factor is obtained by (2.11) through (2.13) as

$$\begin{cases} b_2^N = \frac{K_2^N - K_2^W}{\left(1 - \frac{b_2^W}{b_2^N}\right)} \\ c_2^N = \frac{K_3^N - K_3^W}{\left(1 - \frac{c_2^W}{c_2^N}\right)} \end{cases} \quad (2.11)$$

$$\begin{cases} b_1^N = b_1^W = K_2^N - b_2^N \\ c_1^N = c_1^W = K_3^N - c_2^N \end{cases} \quad (2.12)$$

$$\alpha_D = b_1^N \omega + c_1^N \omega^2 \quad (2.13)$$

As mentioned earlier, β_D can be similarly obtained by the method above.

2.2. EXTRACTION METHOD VALIDATION BY SIMULAITONS

To evaluate this “Root Mean” method, two simulation cases are proposed. One is the smooth conductor and another one is the rough conductor case which are simulated by HFSS 3D simulation tool.

2.2.1. Simulation Validation for Smooth Conductor. Models of two stripline traces of smooth conductor with different widths, but same dielectric medium were built in the HFSS as shown in Figure 2.3 and Figure 2.4. To make sure the full-wave simulations were conducted properly, the simulated results were checked in a few ways. For example, as shown in Figure 2.5, the S-parameters of two 1 inch traces are cascaded and then compared to with the S-parameters of the 2 inch trace with the same cross section. The corresponding ABCD parameters can also be checked. For example, the A and D terms are compared in Figure 2.5. The two parameters shall be the same due to the symmetry.

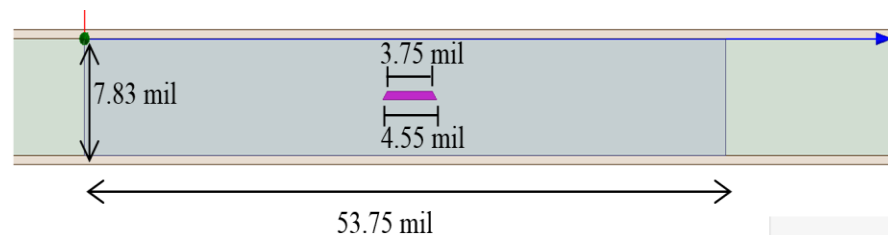


Figure 2.3. Cross section of the narrow trace

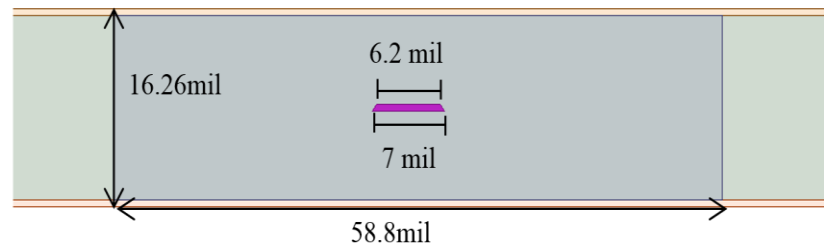


Figure 2.4. Cross section of the wide trace

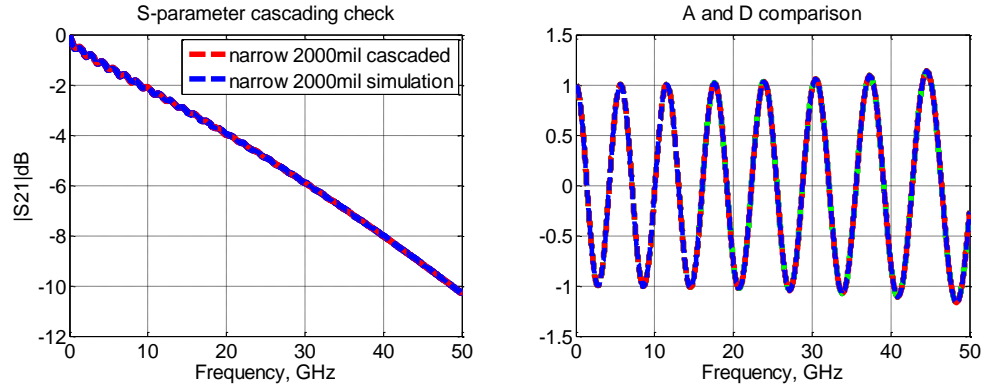


Figure 2.5. Validating simulation results

The DK and DF values were calculated from the simulated S-parameters. Two dielectric materials with different DF values were studied. In each case, traces with two widths and two lengths were simulated. The extracted values are compared in Figure 2.6 and Figure 2.7. Since the conductor surface is assumed to be smooth, the trace width and length shouldn't affect the extracted DK and DF values.

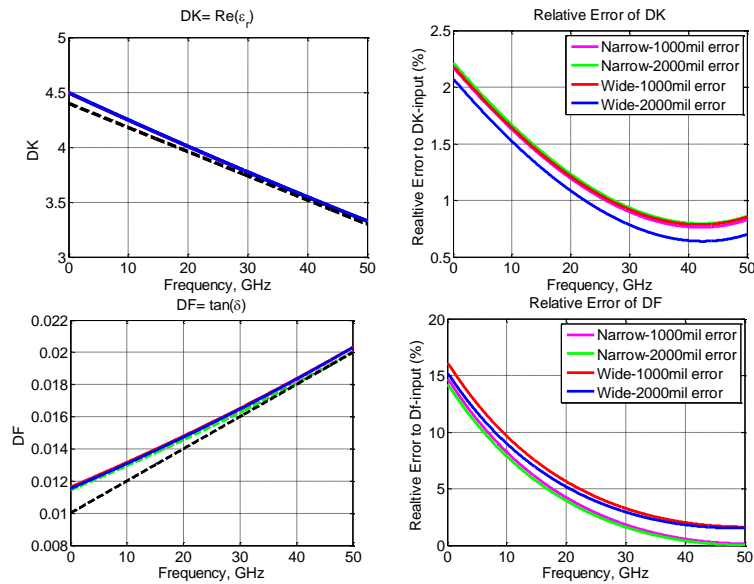


Figure 2.6. DK and DF extraction for a large DF material

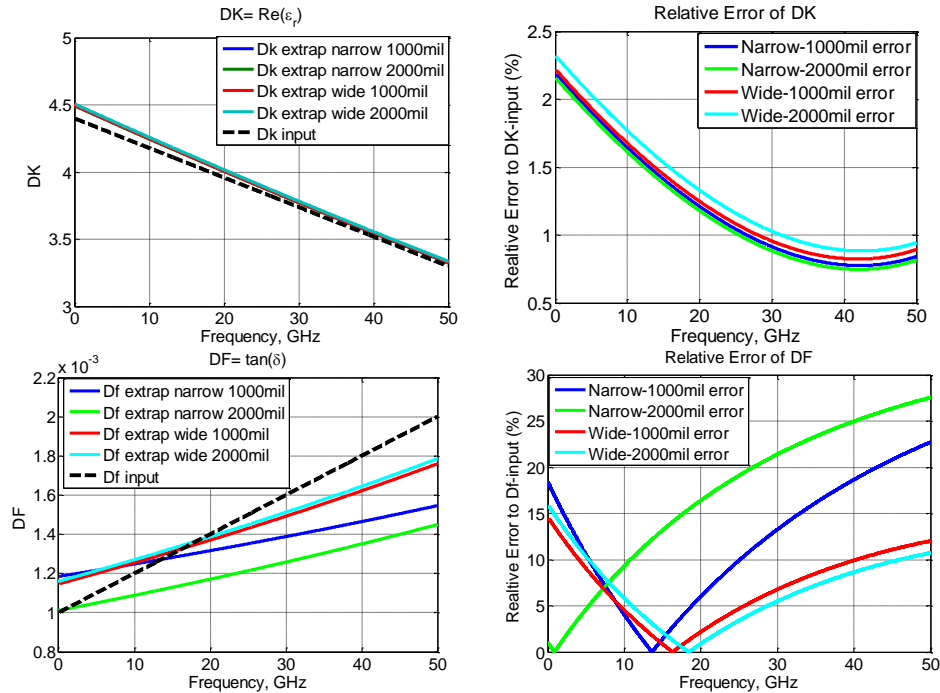


Figure 2.7. DK and DF extraction for a small DF material

It can be seen from the figures that in general the DK extraction works pretty well with a relative error less than 2.5% in the entire frequency band up to 50 GHz for both dielectric materials. In addition, different trace widths and lengths have little impact on the final results. The DK extraction is a different story. The extraction is better for the large loss tangent material, although the relative error at the low frequencies is as high as 15%. For the low loss tangent material, the DF extraction is much worse with larger relative error in general. Further, different trace widths and lengths result in large differences. The simulations have demonstrated that the current DF extraction procedure in the “Root-omega” method needs further improvement. A simple sensitivity analysis will be reported in Section IV to explain why DF is more difficult to be extracted than DK.

From intuitive understanding, in general α_C is larger than α_D . When applying the curve-fitting function to extract α_D , any small error in the curve fitting procedure can result in larger error in the extracted DF value. It is even worse when the DF value is smaller. In the DK extraction, β_D is the dominating term in β_T . Hence, the DK extraction is not significantly affected by the small error in the curve fitting procedure.

2.2.2. Simulation Validation for Rough Conductor. Cross sectional dimensions of two rough traces are shown in Figure 2.8 and Figure 2.9. Based on the ratios calculated from (2.11), DK and DF values were extracted and are shown in Figure 2.10 and Figure 2.11 for two dielectric materials with a large and small loss tangent, respectively. Similar conclusions can be drawn from the simulations. The DK extraction can work well for both cases with a relative error less than 2% in the entire frequency range, while the DF extraction needs further improvement especially for the dielectric material with a smaller loss tangent.

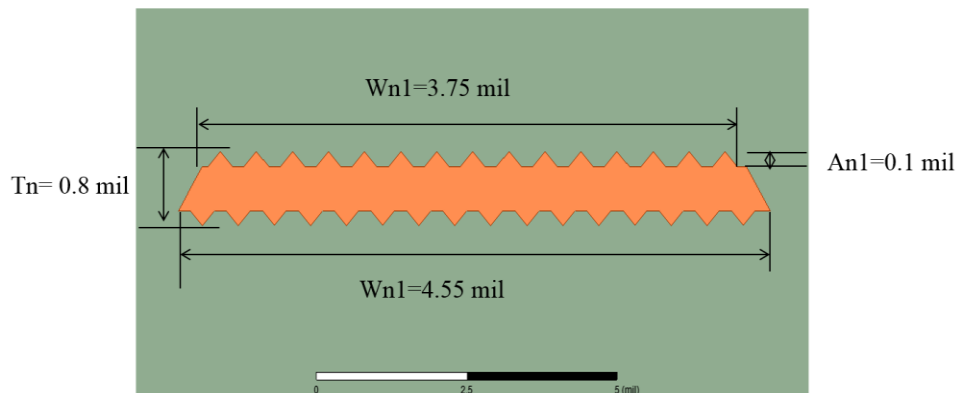


Figure 2.8. Cross section of the rough narrow trace

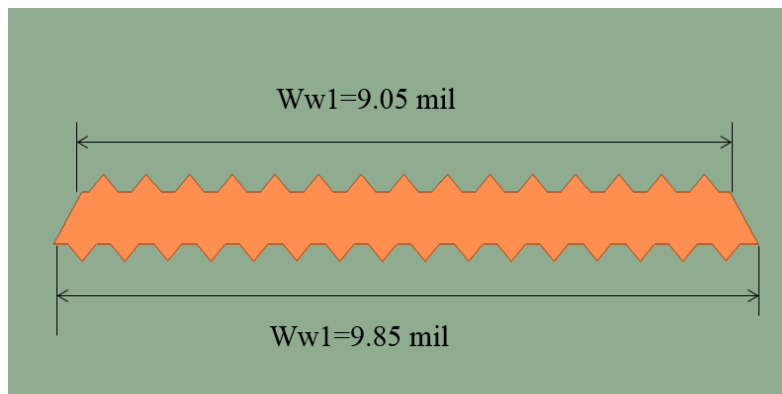


Figure 2.9. Cross section of the rough wide trace

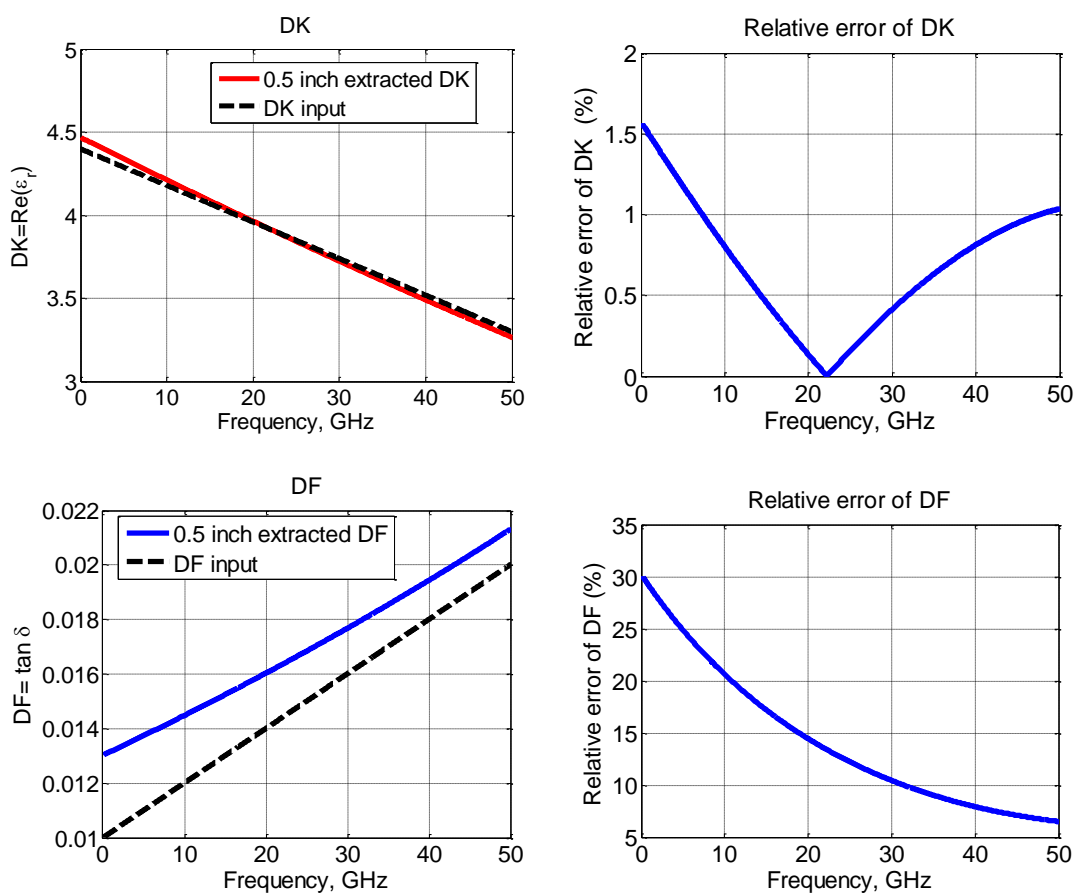


Figure 2.10. DK and DF extraction for a large DF material from two rough traces

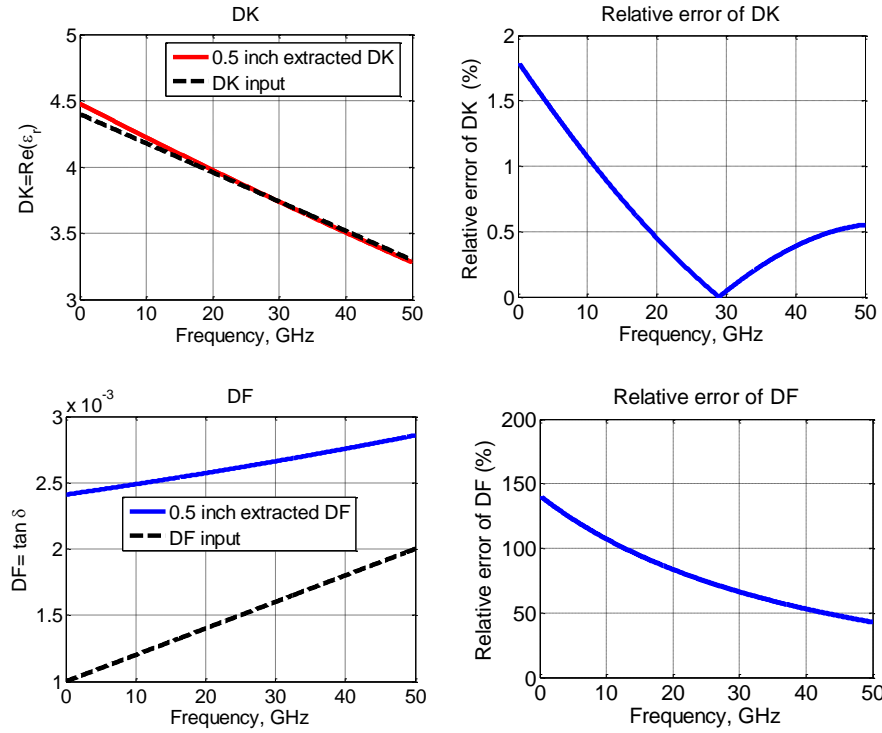


Figure 2.11. DK and DF extraction for a small DF material from two rough traces

2.3. SENSITIVITY ANALYSIS FOR ‘ROOT MEAN’ METHOD

It is shown that the DK extraction has a relatively high accuracy. However, the DF extraction has large errors, and the accuracy becomes even worse for a low loss material. In this section, this phenomenon is explained by performing the sensitivity analysis for the extracted DK and DF.

$$DK = \frac{(v_{free}\beta_D)^2}{\omega^2} \sqrt{\frac{\beta_D^2}{\beta_D^2 + 4\alpha_D^2}} \quad (2.14)$$

$$DF = \frac{2\alpha_D}{\beta_D} \quad (2.15)$$

$$\frac{|\Delta DK|}{DK} = \frac{4\alpha_D}{\beta_D(\beta_D^2 + 4\alpha_D^2)^{3/2}} \Delta\alpha_D + \frac{2(\beta_D^2 + 6\alpha_D^2)}{\beta_D(\beta_D^2 + 4\alpha_D^2)} \Delta\beta_D \quad (2.16)$$

$$\frac{|\Delta DF|}{DF} = \frac{\Delta\alpha_D}{\alpha_D} + \frac{\Delta\beta_D}{\beta_D} \quad (2.17)$$

The DK and DF expressions are listed here again as (2.14) and (2.15) for convenience. Then the sensitivities of DK and DF are derived as in (2.16) and (2.17). As discussed earlier, β_D is the dominating term in β_T while α_D is not in α_T . Then, the errors generated in the curve fitting result in a large $\Delta\alpha_D$ and a small $\Delta\beta_D$. However, in (2.16), the coefficient of $\Delta\alpha_D$ is almost zero. Therefore, the extracted DK is not sensitive to the curve fitting errors. In (2.17), however, the curve fitting errors are directly transferred to the extracted DF value. Therefore, as seen in the simulation results, the extracted DF values are very sensitive to the curve fitting errors.

2.4. INNOVATIVE MATERIAL MODEL DERIVATIONS

To solve the extraction sensitivity problem, we need to study the accurate material model for the extraction procedure. First how to separate the conductor and dielectric loss has to be carefully derived and a causal dielectric model is applied to the dielectric loss calculation. Then a innovative extraction method to combine all the models above to extract the accurate DK, DF and roughness level.

2.4.1. Separation of Conductor and Dielectric Contributions. The theoretical derivation of conductor and dielectric contribution for the loss comes from the famous telegraph equation (2.18).

And in frequency domain equation (2.18) has two tradition circuit model solution, one is the right going wave (RGW) shown in (2.19) and another solution is left going wave (LGW) shown in (2.20).

And the propagation constant $\gamma = \sqrt{(R + j\omega L)(G + j\omega C)}$. And γ is expanded through (2.21) to (2.25) and in (2.24) $\frac{1}{2} \frac{RG}{\omega^2 LC}$ is a second order smaller term which can be neglected compared with other terms.

$$\begin{cases} \frac{d^2 V}{dx^2} = (R + j\omega L)(G + j\omega C)V \\ \frac{d^2 I}{dx^2} = (R + j\omega L)(G + j\omega C)I \end{cases} \quad (2.18)$$

$$RGW \begin{cases} V(x) = V^+ e^{-\gamma x} \\ I(x) = I^+ e^{-\gamma x} \end{cases} \quad (2.19)$$

$$LGW \begin{cases} V(x) = V^- e^{\gamma x} \\ I(x) = I^- e^{\gamma x} \end{cases} \quad (2.20)$$

The propagation constant can be finally expressed as (2.25). The real part of the γ is the attenuation constant α_T and the imaginary part of γ is the phase constant β_T . The equation (2.26) shows the above procedure.

$$\gamma = \sqrt{(R + j\omega L)(G + j\omega C)} \quad (2.21)$$

$$\gamma = \sqrt{RG - \omega^2 LC + j\omega(RC + GL)} \quad (2.22)$$

$$\gamma = j\omega\sqrt{LC} \sqrt{1 - \frac{RG}{\omega^2 LC} - j \frac{RC + GL}{\omega LC}} \quad (2.23)$$

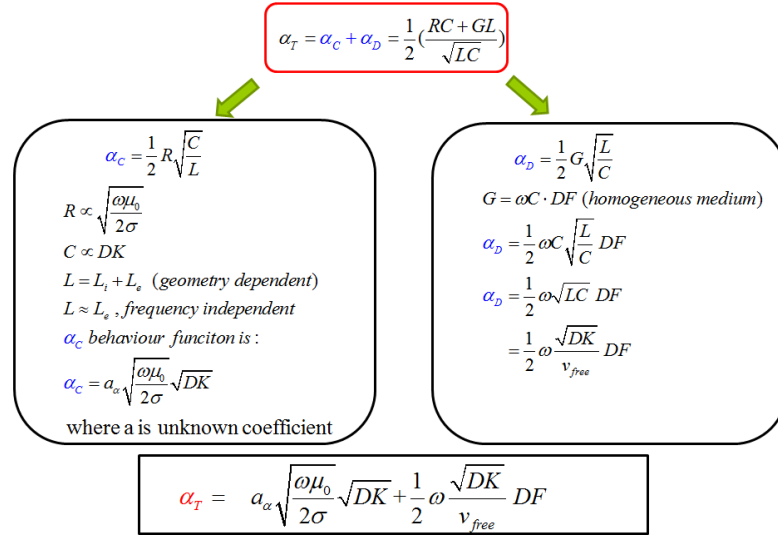
$$\gamma \approx j\omega\sqrt{LC} \left(1 - \frac{1}{2} \frac{RG}{\omega^2 LC} - j \frac{1}{2} \frac{RC + GL}{\omega LC} \right) \quad (2.24)$$

$$\gamma \approx \frac{1}{2} \left(\frac{RC + GL}{\sqrt{LC}} \right) + j\omega\sqrt{LC} \quad (2.25)$$

$$\gamma = \alpha_T + j\beta_T = \frac{1}{2} \left(\frac{RC + GL}{\sqrt{LC}} \right) + j\omega\sqrt{LC} \quad (2.26)$$

$$\boxed{\alpha_T = \frac{1}{2} \left(\frac{RC + GL}{\sqrt{LC}} \right) \quad \beta_T = \omega\sqrt{LC}}$$

Next step it is to separate α_T and β_T into the conductor part and dielectric part which is shown in Figure 2.12 and Figure 2.13.

Figure 2.12. Separate α_T into conductor part and dielectric part

$$\beta_T = \omega \sqrt{LC}$$

$$\beta_T = \omega \sqrt{(L_e + L_i)C}$$

$$\beta_T = \omega \sqrt{L_e C} \sqrt{1 + \frac{L_i}{L_e}} \quad \left(\frac{L_i}{L_e} \ll 1 \right)$$

$$\beta_T \approx \omega \sqrt{L_e C} \left(1 + \frac{L_i}{2L_e} \right)$$

$$\beta_T = \frac{\omega L_i}{2} \sqrt{\frac{C}{L_e}} + \omega \sqrt{L_e C} \quad \text{where } |j\omega L_i| = R_\alpha$$

$$\beta_T = \beta_c + \beta_D$$

$\omega L_i \propto k \sqrt{\omega}$, $C \propto DK$
 L_e is frequency independent

$$\beta_c = a_\beta \sqrt{\frac{\omega \mu_0}{2\sigma}} \sqrt{DK}, \quad \beta_D = \frac{\omega}{v_{free}} \sqrt{DK}$$

$$\beta_T = a_\beta \sqrt{\frac{\omega \mu_0}{2\sigma}} \sqrt{DK} + \frac{\omega}{v_{free}} \sqrt{DK}$$

Figure 2.13. Separate β_T into conductor part and dielectric part

$$\alpha_T = a_\alpha \sqrt{\frac{\omega \mu_0}{2\sigma}} \sqrt{DK} + \frac{1}{2} \omega \frac{\sqrt{DK}}{v_{free}} DF \quad (2.27)$$

$$\beta_T = a_\beta \sqrt{\frac{\omega \mu_0}{2\sigma}} \sqrt{DK} + \frac{\omega}{v_{free}} \sqrt{DK} \quad (2.28)$$

2.4.2. Djordjevic-Sarkar Casual Dielectric Model. The Djordjevic-Sarkar model is a causal dielectric model which is shown in (2.29). The real part (2.30) and imaginary part (2.31) of permittivity are relative to each other.

$$\varepsilon(\omega) = \varepsilon'(\omega) - j\varepsilon''(\omega) = \varepsilon_\infty + \frac{\Delta\varepsilon}{\ln\left(\frac{\omega_B}{\omega_A}\right)} \ln\left(\frac{\omega_B + j\omega}{\omega_A + j\omega}\right) + \frac{\sigma}{j\omega\varepsilon_0} \quad (2.29)$$

$$\text{Real part: } \text{DK} = \varepsilon_\infty + \frac{\Delta\varepsilon}{\ln\left(\frac{\omega_B}{\omega_A}\right)} \ln\left(\frac{\sqrt{\omega_B^2 + \omega^2}}{\sqrt{\omega_A^2 + \omega^2}}\right) \quad (2.30)$$

$$\text{Imaginary part: } \varepsilon''(\omega) = \frac{\Delta\varepsilon}{\ln\left(\frac{\omega_B}{\omega_A}\right)} \ln\left(\frac{\sqrt{\omega_B^2 + \omega^2}}{\sqrt{\omega_A^2 + \omega^2}}\right) \quad (2.31)$$

Because $\tan \delta = \frac{\varepsilon''(\omega)}{\varepsilon'(\omega)}$, at one frequency point ω_1 , the imaginary part of permittivity $\varepsilon''(\omega_1) = \varepsilon_1 \tan \delta_1$. Base on equation (2.31), we can derive that

$$\varepsilon_1 \tan \delta_1 = \frac{\Delta\varepsilon}{\ln\left(\frac{\omega_B}{\omega_A}\right)} \cdot \tan^{-1}\left(\frac{\omega_B}{\omega_1}\right) + \frac{\sigma_{DC}}{\omega_1 \varepsilon_0} \text{ and the slope factor } K \text{ is calculated as (2.31)}$$

$$K = \frac{\Delta\varepsilon}{\ln\left(\frac{\omega_B}{\omega_A}\right)} = \frac{\varepsilon_1 \tan \delta_1 - \frac{\sigma_{DC}}{\omega_1 \varepsilon_0}}{\tan^{-1}\left(\frac{\omega_B}{\omega_1}\right)} \quad (2.32)$$

This slope is directly calculated by ε_1 , $\tan \delta_1$, ω_1 , ω_B and σ_{DC} is almost zero which can be neglected.

At frequency ω_1 , the real part of permittivity can be shown as

$$\left\{ \begin{array}{l} \varepsilon_1 = \varepsilon_\infty + \frac{\Delta\varepsilon}{\ln\left(\frac{\omega_B}{\omega_A}\right)} \ln\left(\frac{\sqrt{\omega_B^2 + \omega_1^2}}{\sqrt{\omega_A^2 + \omega_1^2}}\right) \\ \varepsilon_1 \cong \varepsilon_\infty + \frac{\Delta\varepsilon}{\ln\left(\frac{\omega_B}{\omega_A}\right)} \ln\left(\frac{\sqrt{\omega_B^2 + \omega_1^2}}{\omega_1}\right) \\ \varepsilon_1 = \varepsilon_\infty + K \cdot \ln\left(\frac{\sqrt{\omega_B^2 + \omega_1^2}}{\omega_1}\right) \end{array} \right. \quad (2.33)$$

$$\varepsilon_\infty = \varepsilon_1 - K \cdot \ln\left(\frac{\sqrt{\omega_B^2 + \omega_1^2}}{\omega_1}\right) \quad (2.34)$$

So the high-frequency permittivity is expressed in (2.34) and it is calculated by ε_1 , ω_1, ω_B and K from (2.32). And base on equation (2.30), (2.32) and (2.34), DK can be finally derived as

$$DK = \varepsilon_1 \left\{ 1 - \frac{\tan \delta_1}{\tan^{-1}(\omega_\infty/\omega_1)} \ln\left(\frac{\sqrt{\omega_\infty^2 + \omega_1^2}}{\omega_1}\right) + \frac{\tan \delta_1}{2\tan^{-1}(\omega_\infty/\omega_1)} \ln\left(\frac{\omega_\infty^2 + \omega^2}{\omega_A^2 + \omega^2}\right) \right\} \quad (2.35)$$

The DK in the whole frequency band can be described by at one specified frequency point DK value, which is shown in (2.35). And base on the

equation $\tan \delta = \frac{\varepsilon''}{\varepsilon'}$, $\varepsilon'' = \frac{K \cdot \tan^{-1}\left(\frac{\omega_B}{\omega}\right)}{DK}$, DF in the interested frequency band be calculated

similarly.

2.4.3. Huray Model for Surface Roughness. It has be derived in (2.27) and

$$(2.28) \text{ that } \alpha_T = a_\alpha \sqrt{\frac{\omega \mu_0}{2\sigma}} \sqrt{DK} + \frac{1}{2} \omega \frac{\sqrt{DK}}{v_{free}} DF \quad \text{and} \quad \beta_T = a_\beta \sqrt{\frac{\omega \mu_0}{2\sigma}} \sqrt{DK} + \frac{\omega}{v_{free}} \sqrt{DK} \quad .\text{And}$$

surface roughness contributes to AC resistance of the conductor, which is corresponding to conductor loss α_C . So α_T is refined with Huray model (2.36) as shown in equation (2.37). Similarly impedance of internal inductance is proportional to AC resistance and β_C is multiplied with Huray factor and β_T is redefined in equation (2.38).

$$\text{Huray Factor(HF)} = \left(\frac{1 + K_1}{1 + \left(\frac{\omega}{\omega_1}\right)^{-\frac{1}{2}} + \frac{1}{2} \left(\frac{\omega}{\omega_1}\right)^{-1}} \right) \quad (2.36)$$

$$\alpha_T = \frac{1}{2} \frac{\omega \cdot DF}{v_{free}} \sqrt{DK} + a_\alpha \sqrt{\frac{\omega \mu_0}{2\sigma}} \cdot \text{HF} \cdot \sqrt{DK} \quad (2.37)$$

$$\beta_T = \frac{\omega \cdot \sqrt{DK}}{v_{free}} + a_\beta \sqrt{\frac{\omega \mu_0}{2\sigma}} \cdot \text{HF} \cdot \sqrt{DK} \quad (2.38)$$

With extracted DK, DF values and cross-section geometry, the smooth conductor is simulated by Intel tool. Then calculate the smooth conductor loss as

$$\alpha_{Csmooth} = \alpha_T - \alpha_D = \alpha_T - \frac{1}{2} \frac{\omega \cdot DF}{v_{free}} \sqrt{DK} \quad .\text{And base on the Huray roughness level extraction}$$

equation (2.39) to extract the roughness level.

$$\text{Huray Factor} : \left(\frac{1 + N \cdot K_{single}}{1 + \left(\frac{\omega}{\omega_1}\right)^{-\frac{1}{2}} + \frac{1}{2} \left(\frac{\omega}{\omega_1}\right)^{-1}} \right) = \frac{\alpha_T - \frac{1}{2} \frac{\omega \cdot DF}{v_{free}} \sqrt{DK}}{\alpha_{Csmooth}} \quad (2.39)$$

$$\beta_{T_DD} = \frac{\omega \cdot \sqrt{DK}}{V_{\text{free}}} + a_{DD} \sqrt{\frac{\omega \mu_0}{2\sigma}} \left(1 + K_i \frac{1}{1 + \left(\frac{\omega}{\omega_i}\right)^{\frac{1}{2}} + \frac{1}{2} \left(\frac{\omega}{\omega_i}\right)^{-1}} \right) \sqrt{DK} \quad (2.40)$$

$$\beta_{T_CC} = \frac{\omega \cdot \sqrt{DK}}{V_{\text{free}}} + a_{CC} \sqrt{\frac{\omega \mu_0}{2\sigma}} \left(1 + K_i \frac{1}{1 + \left(\frac{\omega}{\omega_i}\right)^{\frac{1}{2}} + \frac{1}{2} \left(\frac{\omega}{\omega_i}\right)^{-1}} \right) \sqrt{DK} \quad (2.41)$$

$$\frac{\beta_{T_DD} - \frac{\omega \sqrt{DK}}{V_{\text{free}}}}{\beta_{T_CC} - \frac{\omega \sqrt{DK}}{V_{\text{free}}}} = \frac{a_{DD}}{a_{CC}} = R \quad (2.42)$$

$$\beta_{T_DD} = R \beta_{T_CC} - \frac{\omega \sqrt{DK}}{V_{\text{free}}} (R - 1) \quad (2.43)$$

As shown in the extraction flow chart, by using the non-linear fitting which treat (2.42) as goal function, DK and DF value at one frequency point can be obtained. Then the whole frequency bank DK and DF can be calculated by (2.35). And here we need to emphasize that the fitting boundary is very important for the accurate extraction.

And the ration boundary can be calculated by roughly get the R,L,G,C terms from the S-parameters and then convert it to conductor loss. And then tune the DK and DF value at 1GHz to get the up boundary of them. After that we can use the extracted DK and DF in whole frequency band to calculate the ratio boundary. Then the up boundary of DK, DF, ratio can be used to do the non-linear fit to extract the DK and DF value that we are interested.

2.5. MEASUREMENT AND RESULTS COMPARISON

As the extraction model and method have been studied, next step is to test this whole extraction procedure. Several test boards are measurement to validate this new method.

2.5.1. Test Board Geometries. In order to validate the proposed new extraction method, lots of measurement of PCB boards with different dielectric material properties has be done. Basically there are three kinds of test boards as shown below. First one is the test coupon provide by Intel side as shown in Figure 2.15. To extract the transmission line behavior, the SFD(Smart Fixture De-embedding) technology is applied to the two test patterns.

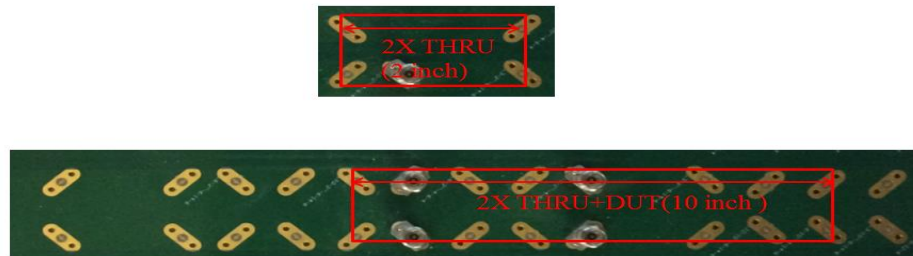


Figure 2.15. Intel's VLP test board

And the cross-section information is illustrated in Figure 2.16. The trace width is 4 mils, trace space is 6 mils and trace thickness is 1.3 mils. Another test board is provided by Cisco which foil type is VLP2. The board geometry and cross-section information is shown in Figure 2.17 and Figure 2.18 respectively. And we will also use the geometry information as the input to simulate the differential S-parameters to compare with the measurement results. However, when the DK and DF are extracted from the whole procedure, the geometry information is not needed.

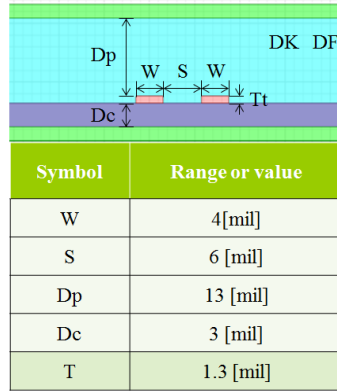


Figure 2.16. Cross-section of the VLP test board

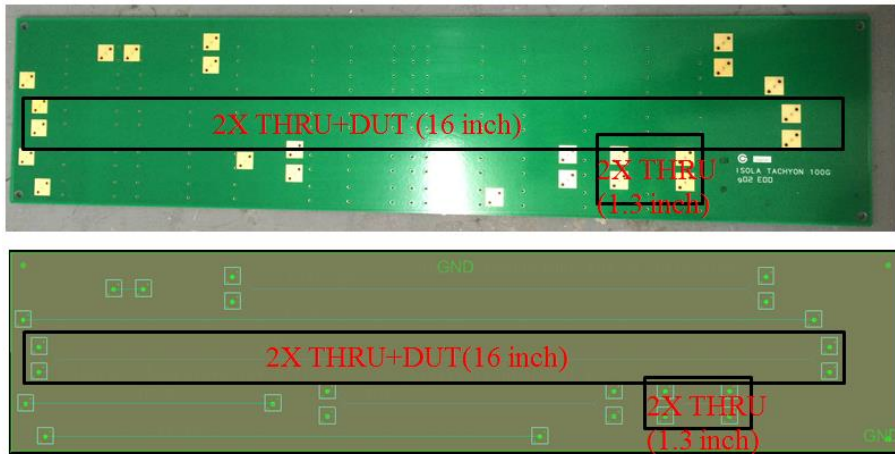


Figure 2.17. Cisco's VLP2 test board

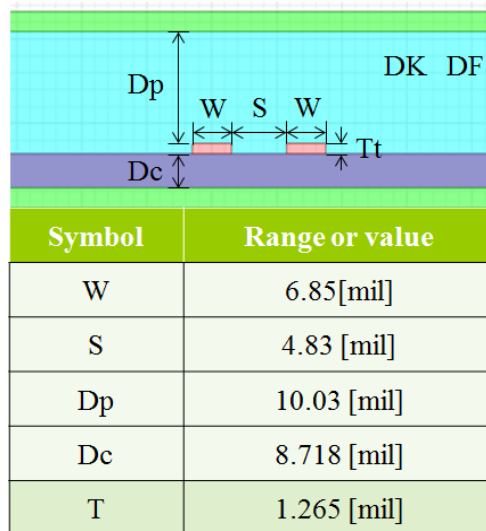


Figure 2.18. Cross-section of the VLP2 test board

The third test board is also provided by Cisco, which is the PCIe board. The board geometry and cross-section information is shown in Figure 2.19 and Figure 2.20 respectively. The 2X through is 4 inch length and the total is 6 inch length, so the final DUT is 2 inch length.

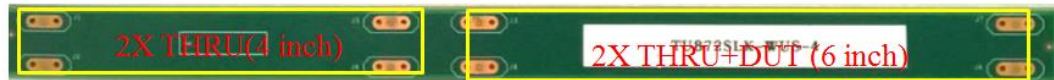


Figure 2.19. Cisco's PCIe test board

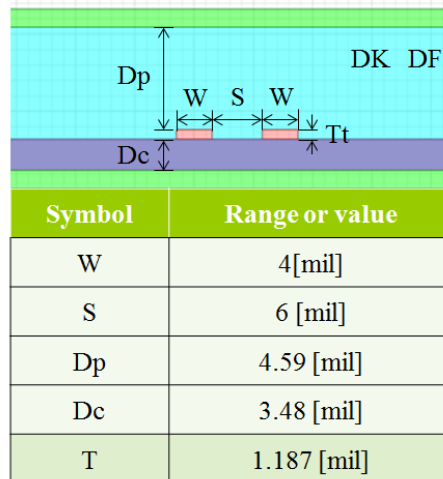


Figure 2.20. Cross-section of the PCIe test board

2.5.2. Measurement Set Up. The 4 port PNA shown in Figure 2.21 is used to measure the differential stripline, which has the frequency band up to 50 GHz. The PNA set up is illustrated on left side of Figure 2.21.

Frequency range: 10MHz~50GHz
 Power: 0dB m
 If bandwidth: 10KHz
 Average: 64



Figure 2.21. Four-port PNA with frequency band up to 50GHz

2.5.3. Extraction Results Compared with Measurement Data. Once the mixed mode S-parameters have been obtained, they are loaded into the material extraction tool shown in Figure 2.22 and trace length and cross-section stack-up information are also needed for the input. Then the DK, DF and Huray roughness level will be extracted, which will be later loaded into Intel's 2D simulation tool to get the simulated S-parameters. Finally the simulated S4P will compare with the measurement data to validate the extraction method.

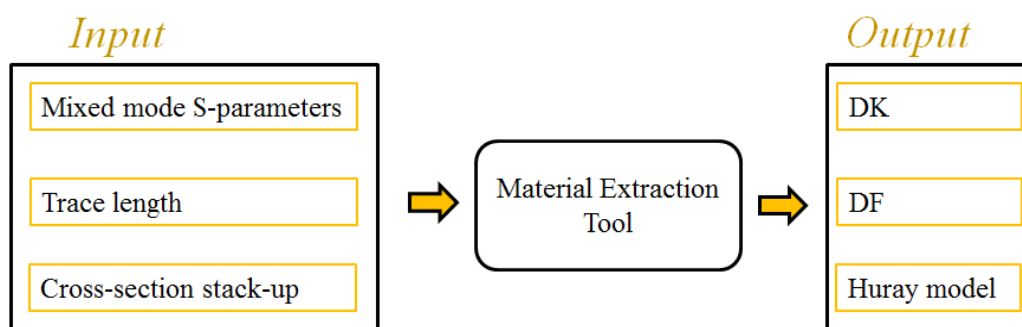


Figure 2.22. Material characterization flow chart

2.5.3.1 DK and DF extraction from intel VLP board measurement. The extracted material properties are shown in Figure 2.23. The extracted DK at 1GHz is 4.45 and extracted DF at 1GHz is 0.0101. The Huray snow ball number is 41 and load the extracted data into 2D simulation tool to make the comparison with measurement data.

| Intel board 4-6-4 | DK at 1GHz | DF at 1GHz |
|------------------------|------------|-------------|
| VLP Layer 10 Vendor | 4.1~4.2 | 0.007~0.009 |
| VLP Layer 10 Extracted | 4.048 | 0.0101 |

Figure 2.23. Intel VLP board extraction results

Figure 2.24 and Figure 2.25 show differential mode magnitude and phase comparison .Both magnitude and phase match well up to 20GHz.The largest discrepancy of magnitude is with 1dB for the 8inch stripline.

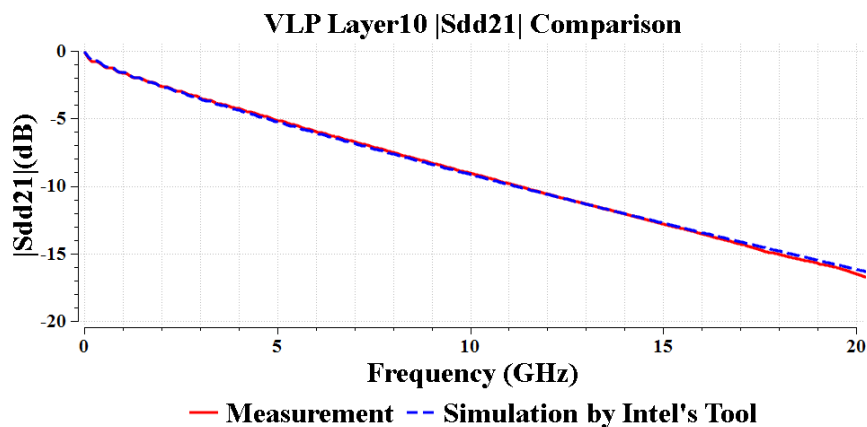


Figure 2.24. Sdd21 magnitude comparison of Intel board

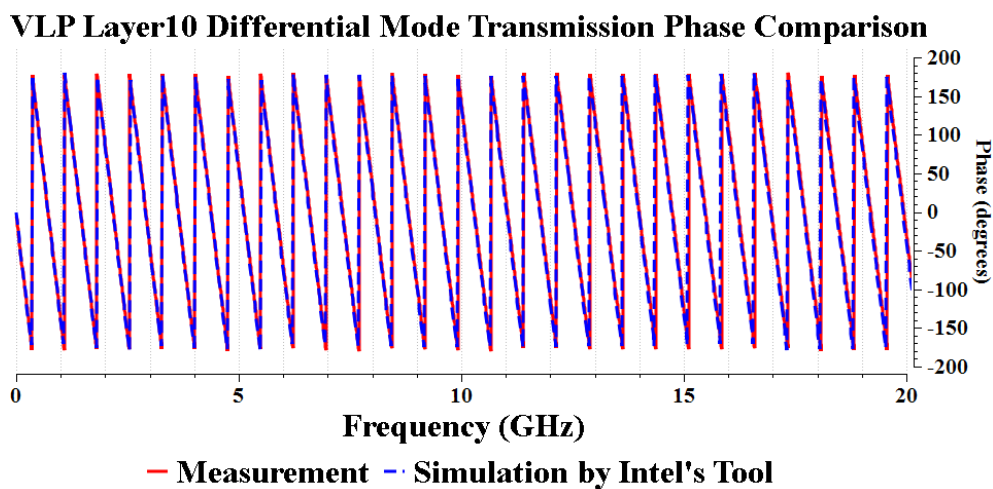


Figure 2.25. Sdd21 phase comparison of Intel board

And the S21 matches well means that the extracted DF is good and the phase information means that the DK results are pretty good. In the future , up frequency will need to push to 30GHz or higher.

Figure 2.26 and Figure 2.27 show common mode magnitude and phase comparison .Both magnitude and phase match well up to 20GHz.The largest discrepancy of magnitude is with 1dB for the 8inch DUT.

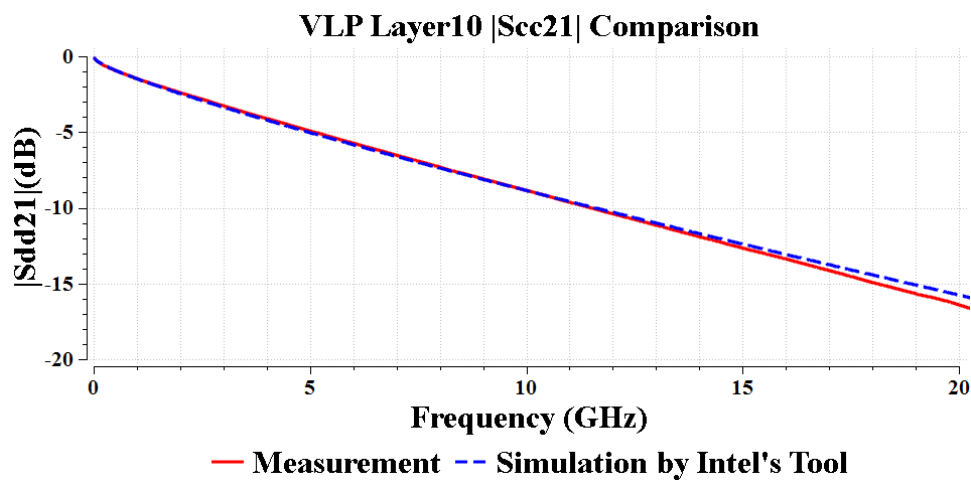


Figure 2.26. Scc21 magnitude comparison of Intel board

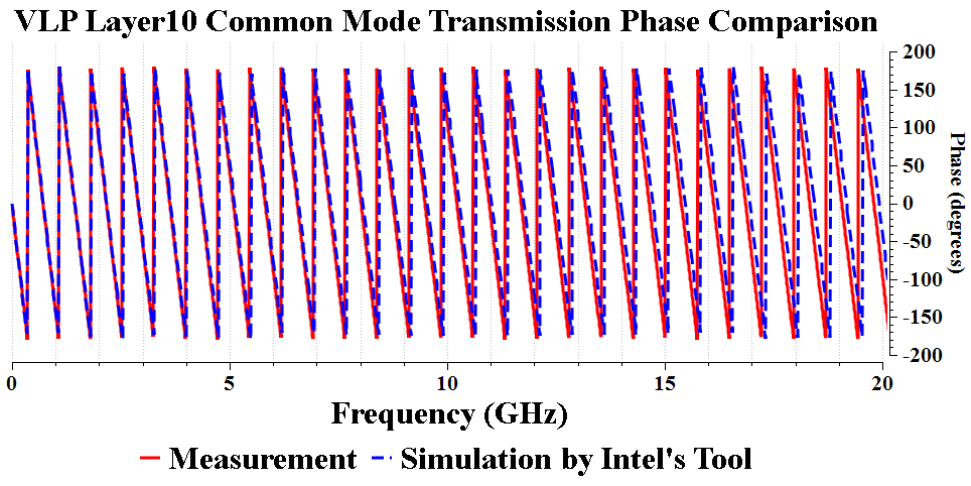


Figure 2.27. Scc21 phase comparison of Intel board

And the S21 matches well means that the extracted DF is good and the phase information means that the DK results are pretty good. In the future , up frequency will need to push to 30GHz or higher.

2.5.3.2 DK and DF extraction from cisco VLP2 board measurement. The extracted material properties are shown in Figure 2.28. The extracted DK at 1GHz is 3.35 and extracted DF at 1GHz is 0.0029. The Huray snow ball number is 39 and load the extracted data into 2D simulation tool to make the comparison with measurement data.

| Cisco board VLP2 | DK at 1GHz | DF at 1GHz |
|------------------------|------------|------------|
| Tachyon 100G Vendor | 3.25 | 0.0022 |
| Tachyon 100G Extracted | 3.351 | 0.0029 |

Figure 2.28. Cisco VLP2 board extraction results

Figure 2.29 and Figure 2.30 show differential mode magnitude and phase comparison .Both magnitude and phase match well up to 20GHz. Figure 2.31 and Figure 2.32 show common mode magnitude and phase comparison .Both magnitude and phase match well up to 20GHz.

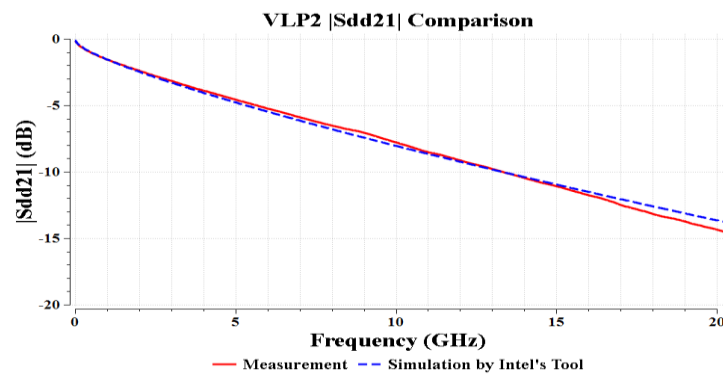


Figure 2.29. Sdd21 magnitude comparison of Cisco VLP2 board

And the S21 matches well means that the extracted DF is good and the phase information means that the DK results are pretty good.

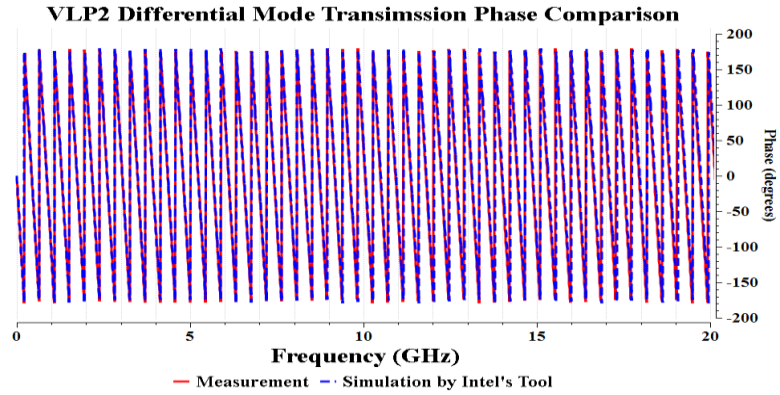


Figure 2.30. Sdd21 phase comparison of Cisco VLP2 board

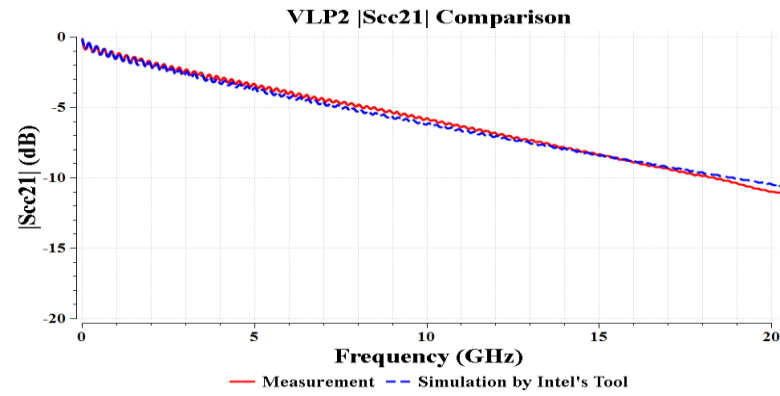


Figure 2.31. Scc21 magnitude comparison of Cisco VLP2 board

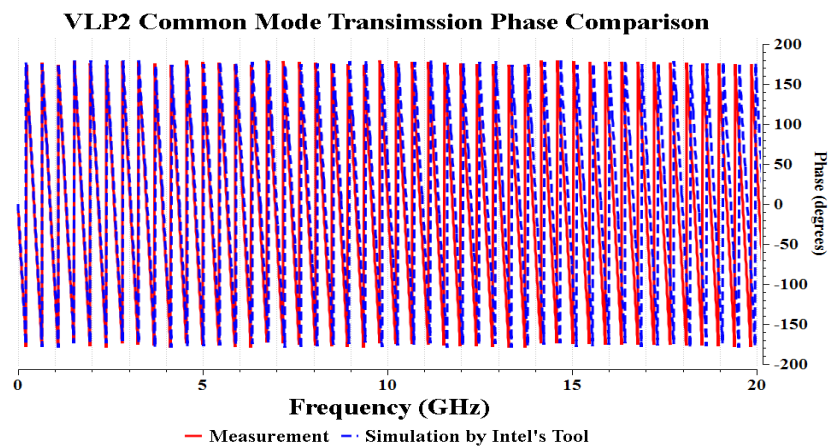


Figure 2.32. Scc21 phase comparison of Cisco VLP2 board

2.5.3.3 DK and DF extraction from cisco PCIe board measurement. The extracted material properties are shown in Figure 2.33. The extracted DK at 1GHz is 3.91 and extracted DF at 1GHz is 0.0082. The Huray snow ball number is 50. Figure 2.34 and Figure 2.35 show differential mode magnitude and phase comparison.

| Cisco PCIe board | DK at 1GHz | DF at 1GHz |
|-------------------------|------------|------------|
| RTF TU872 SLK Vendor | 4.01 | 0.01 |
| RTF TU872 SLK Extracted | 3.91 | 0.0082 |

Figure 2.33. Cisco PCIe board extraction results

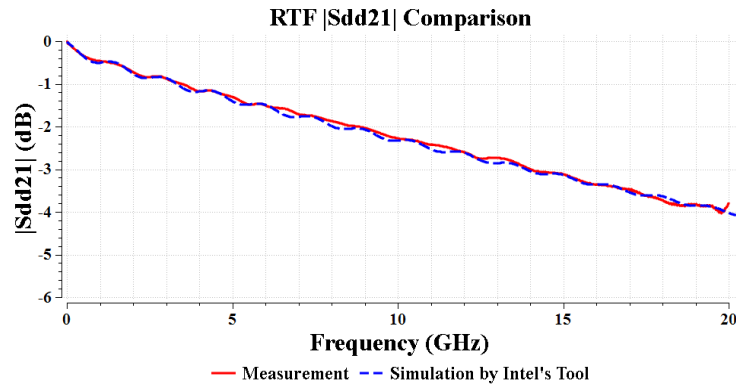


Figure 2.34. Sdd21 magnitude comparison of Cisco PCIe board

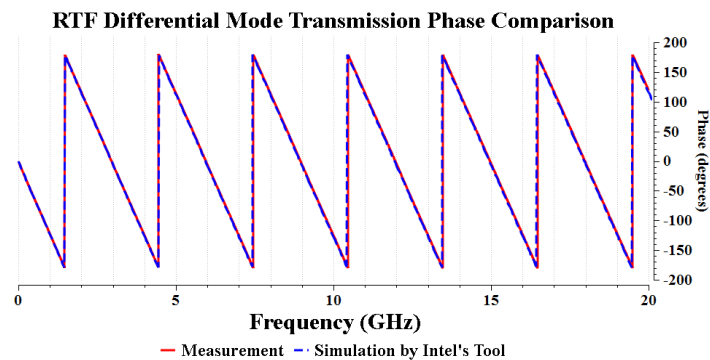


Figure 2.35. Sdd21 phase comparison of Cisco PCIe board

Figure 2.36 and Figure 2.37 show common mode magnitude and phase comparison. Both magnitude and phase match well up to 20GHz. The largest discrepancy of magnitude is with 1dB for the 2 inch DUT.

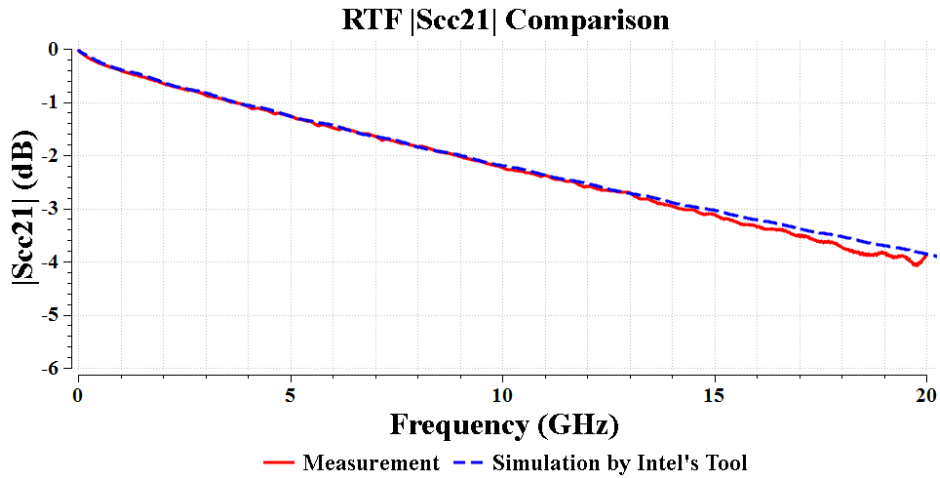


Figure 2.36. Scc21 magnitude comparison of Cisco PCIe board

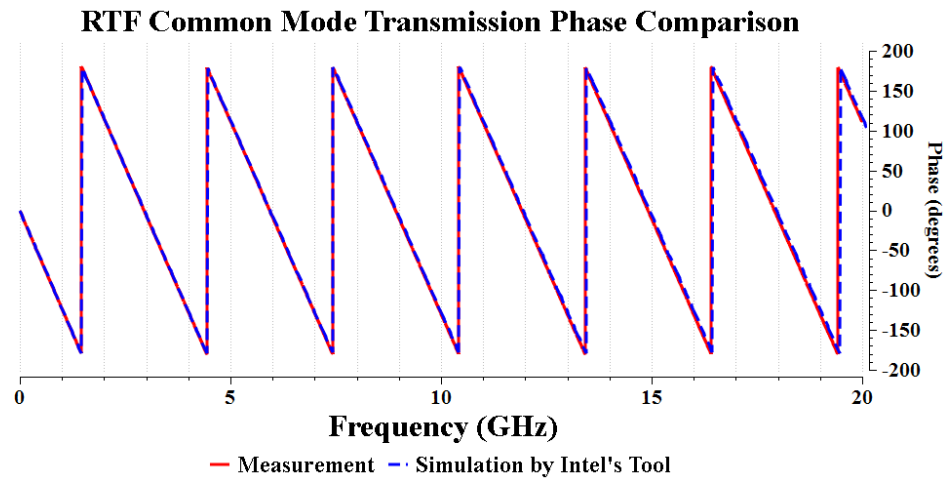


Figure 2.37. Scc21 phase comparison of Cisco PCIe board

3. PEEC MACROMODELS FOR ABOVE PLANE DECOUPLING CAPACITORS

3.1. MODELING OF L-ABOVE

Conventionally, the model for the inductance of the decoupling capacitors is specified for the capacitors alone [14]. The problem is that the impedance of the above plane decoupling capacitor model is highly influenced by the connections and other mounting details such as the distance to the nearest ground plane, which is shown in Figure 3.1. Hence, even a good PEEC equivalent circuit for the capacitor itself is insufficient since all the couplings to the mounting environment must be taken into account. For this reason, we pick a reasonable connection structure to the capacitor.

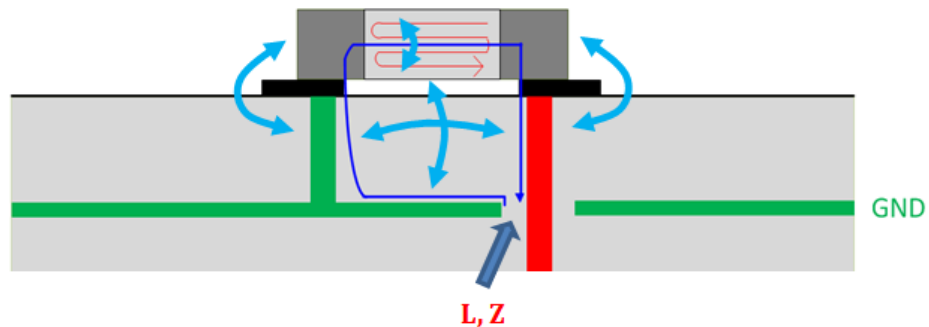


Figure 3.1. Decoupling capacitor's mounting environment

The internal structure of most high capacitance decoupling capacitors consists of multiple layers. Representing all the layers would be computationally expensive. To keep the compute time reasonably low, we use the simplified 3 layer model shown in Figure 3.2 such that the main properties of the model are preserved like the capacitor resistance R – also known as ESR. This value is less dependent on the environment than other element values. However, R is in general dependent on frequency [14]. We note that the PEEC preserves the frequency dependence. A model is needed which includes the strong

couplings to the local PDN system. Hence, the model needs to include these additional local connections. Figure 3.3 shows connections where the capacitor is connected to the 20×20 mil pads. The connections to the macromodel are established to the 10×10 mil pads via wires or vias. Also shown is a plane which usually is located 5 mils to 30 mils underneath the contacts. An important quantity in the model is the distance between the capacitor plates and the contacts which we measured to be 9 mils.

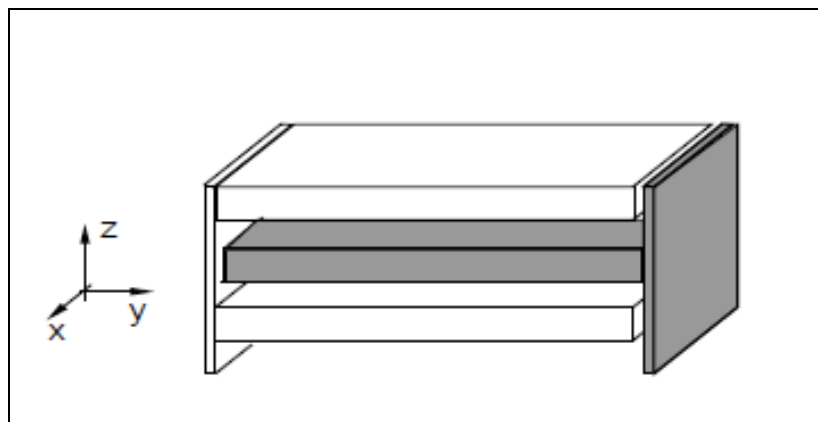


Figure 3.2. Simplified three layer model for decoupling capacitors

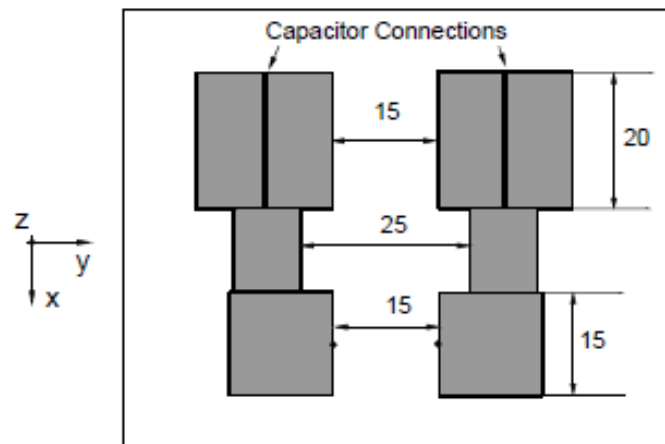


Figure 3.3. Top view of connections to the capacitor with ground plane underneath

The result we are looking for is a simple capacitor environment which can be used for the PDN analysis to reduce complexity of the overall models. However, the PEEC model must take all the local couplings into account between the capacitor in Figure 3.2 and the connections in Figure 3.3 as well as the ground plane underneath. Of course, the coupling of the capacitor macromodel to the rest of the PDN system must be weak.

3.2. PEEC MODELS FOR DISTRIBUTED AND LUMPDED MODELS

The transformation of the EM model into PEEC equivalent circuits has been published in many papers, e.g., [15]. Hence, we present only the issues which are key for this short paper. For the PDN model, frequency content from DC to 2 GHz covers the spectrum of interest. Hence, a quasi-static PEEC model is sufficient for the decoupling capacitors, which can be assumed to be smaller than 1 cm, which means less than $\lambda/10$ for $f_{\max} = 15$ cm.

The PEEC model used is based on the total electric field inside of a conductor is given by

$$\mathbf{E}(r,t) = \frac{\mathbf{J}(r,t)}{\sigma} - \frac{\partial \mathbf{A}(r,t)}{\partial t} - \nabla \Phi(r,t) \quad (3.1)$$

where in our case $\mathbf{E}^i(r,t) = 0$ since we assume that the applied electric field is zero. Further, $\mathbf{J}(r,t)$ is the current density in the conductors and $\mathbf{A}(r,t), \Phi(r,t)$ are the vector and scalar potentials respectively and σ is the electrical conductivity. The second MNA equation is derived in its conventional form in the frequency domain as

$$\mathbf{A}^T \mathbf{V}(s) + (\mathbf{R} + s\mathbf{L}p) \mathbf{I}(s) = 0 \quad (3.2)$$

For the first MNA equation, we want to represent the high permittivity between the inner layers shown in Figure 3.4 (a) with the lumped inter-layer capacitances shown in Figure 3.4 (b).

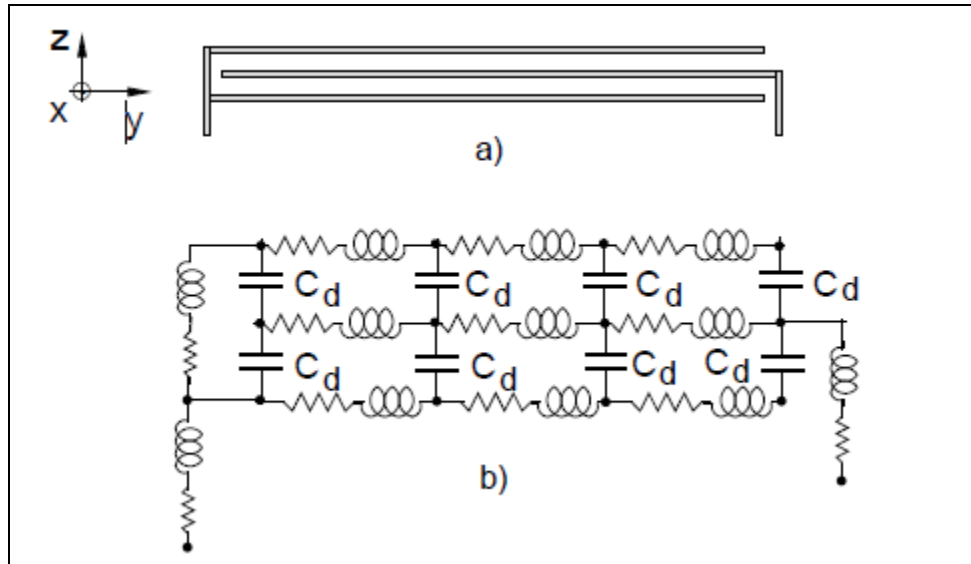


Figure 3.4. Side view of simplified cross-section model (a)
Simple layer of combined lumped capacitor and distributed PEEC model (b)

The sum of all N internal layer capacitors is

$$\sum_{k=1}^N C_{d,k} = ESC \quad (3.3)$$

where ESC is the value of the capacitance. The conductivity σ of the plated in Figure 3.4 is chosen to represent the vendor specified resistance ESR of the capacitor. Here, we assume that a short exists at the center in the y -direction between the outside of the plates and the center conductor.

Finally, we can set up the MNA equations for the model. The resultant pcEFIE (potential-charge) integral equation is best described in the circuit domain by the MNA equations in terms of the node potentials $\Phi(s)$ and the source currents $I_s(s)$

$$[\mathbf{M}] = \begin{bmatrix} \Phi(s) \\ I_l(s) \end{bmatrix} = \begin{bmatrix} I_s(s) \\ 0 \end{bmatrix} \quad (3.4)$$

where the circuit matrix is

$$[\mathbf{M}] = \begin{bmatrix} s(\mathbf{A}_d \mathbf{C}_d \mathbf{A}_d^T + \mathbf{P}p^{-1}) & -\mathbf{A}_l \\ -\mathbf{A}_l^T & -(\mathbf{R} + s\mathbf{L}p) \end{bmatrix} \quad (3.4)$$

The incidence matrices \mathbf{A} can also be called matrix Kirchhoff current laws. Specifically, \mathbf{A}_l is the matrix for the partial inductance connections. Also, \mathbf{A}_d Ad represents the matrix KCL for the dielectric capacitances \mathbf{C}_d for the dielectrics. Hence, this is used to insert lumped capacitances \mathbf{C}_d into the PEEC circuit.

We should note that all the non-orthogonal partial inductances are coupled. This results in important inductive couplings between the capacitor in Figure 3.2, the connections in Figure 3.3 as well as the ground plane. The result obtained without these couplings is inaccurate. Hence, the ESL value specified by a manufacturer only gives an order of magnitude estimate. The terminals in Figure 3.3 represent a much better location for partitioning the system.

An assumption concerning the accuracy of the model is based on the loop opening between the terminal connections in Figure 3.3 where the model is connected to the rest of the PDN circuit. The distance between the terminals needs to be small enough such that only a small fraction of the total inductance is not included between the terminals.

3.3. NUMERICAL AND TEST RESULTS

This stage we only consider the modeling of a 0402, 1 μ F decoupling capacitor with the connection model such that a partitioned macromodel can be defined. The couplings between the local connections have a large impact on the circuit model used for the capacitor. Hence, we tested the macromodel unit consisting of the capacitor in Figure 3.2 connected to the interconnects in Figure 3.3. We should note that the inductance in the macromodel does not have a relation to the ESL inductance value specified for capacitor mainly due to the partial inductance which is absent in this model.

Our first test represents the hybrid PEEC-circuit model for the capacitor shown in Figure 3.4. The first test checks how the number of discrete capacitors C_d representing the high value dielectrics impacts the response of the macromodel in Figure 3.5. We also observe that 14 capacitors which are uniformly distributed between the plates give a good answer even for the parallel resonance observed at about 90MHz.

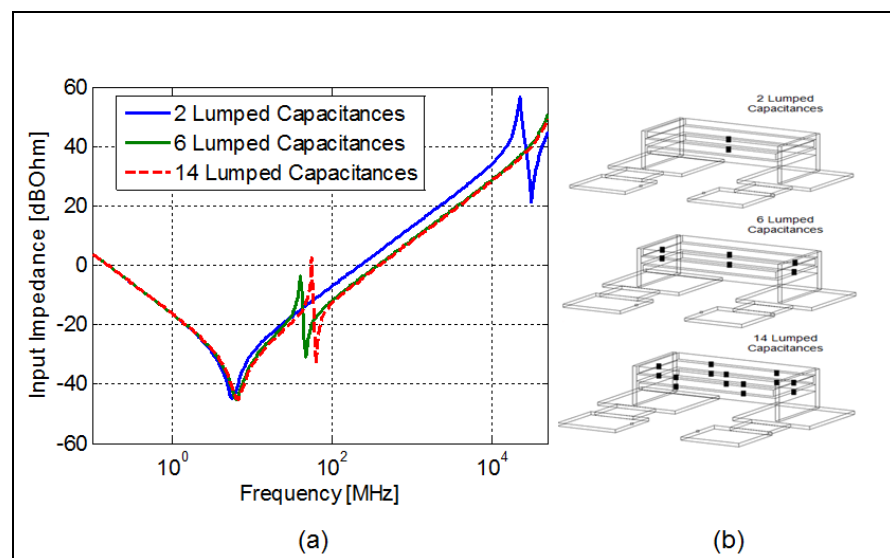


Figure 3.5 Response as a function of the number of C_d capacitances (a)
Distribution of the lumped capacitance (b)

Next, we consider the impact of the ground plane under the capacitor macromodel, which are 5 mils for close planes and to 30 mils for planes which are further away. Figure 3.6 shows the behavior of the macromodel in the frequency range of interest also as a function of the ground plane spacing which is computed using the PEEC model. These inductances are derived as a simple model at about 500MHz. These calculations show that the macromodel must be specified as a function of the ground plane distance as the most important parameter, which is shown in Figure 3.7.

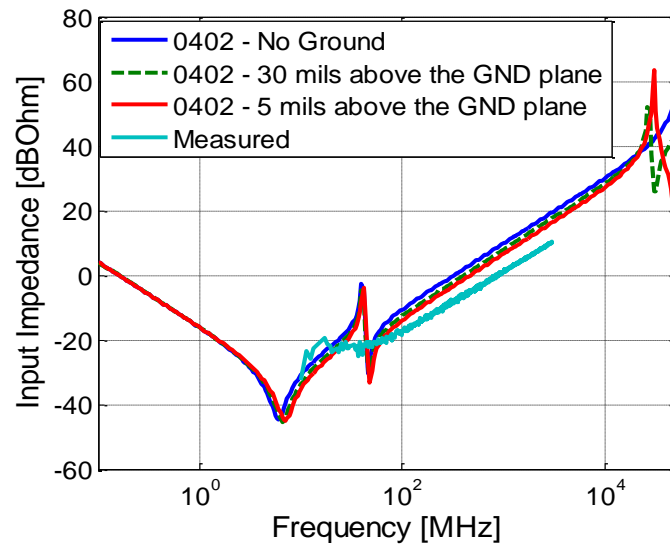


Figure 3.6. Approximate inductance of the model for different ground plane

TABLE I
COMPARISON OF MACROMODEL INDUCTANCES

| Model Details | Spacing to ground | Total Inductance |
|---------------------------|-------------------|------------------|
| Measured result | 5 mils | 0.17 nH |
| With ground plane | 5 mils | 0.34 nH |
| With ground plane | 30 mils | 0.39 nH |
| No ground under capacitor | ∞ | 0.57 nH |

Figure 3.7. Table of macromodel inductances of different ground plane distance

However, the probes were placed close to the center part of the connections in Figure 3.3. The measured resonance effect in the measurement in Figure 3.6 shows the presence of the parallel resonance. However, the damping is strong due to the dielectric loss [14]. In Figure 3.8, one pole Debye is added in EM PEEC modeling.

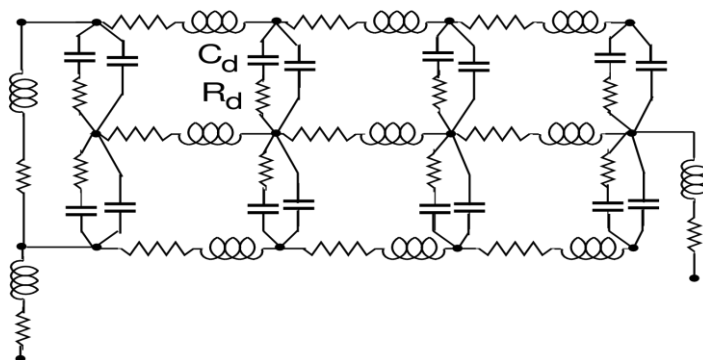


Figure 3.8. Single pole Debye model for lossy dielectric

As shown in Figure 3.9 that the resonance on red curve is damped by adding the Debye lossy model which is more close to the measurement results. In the future we will adding more lumped capacitors to speed up the solution, also the higher order Debye model will be studied.

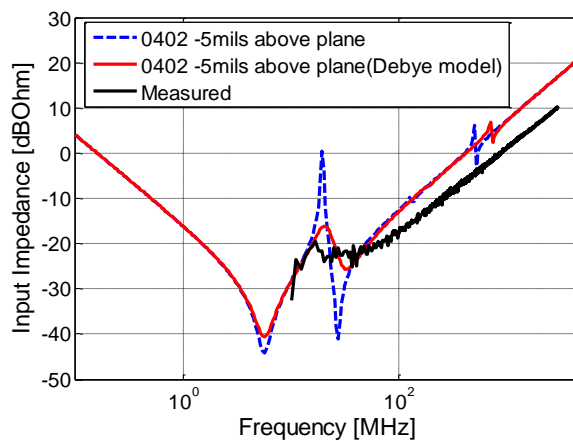


Figure 3.9. Comparison of mode with and without loss

The input impedance obtained from the PEEC solution can be synthesized into an appropriate circuit macromodel for the frequency range of interest. We note that the connection terminals to the model form an open loop. However, the distance is sufficiently small such that the error is also small.. Finally, we show that the circuit model in Figure 3.10 with the parallel circuit part leads to the red dotted response in Figure 3.11 which is a good approximate simpler macromodel

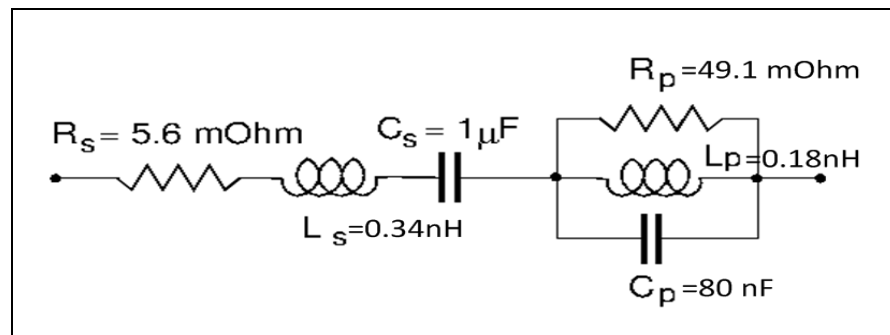


Figure 3.10. Macromodel which includes parallel resonance and loss dielectric

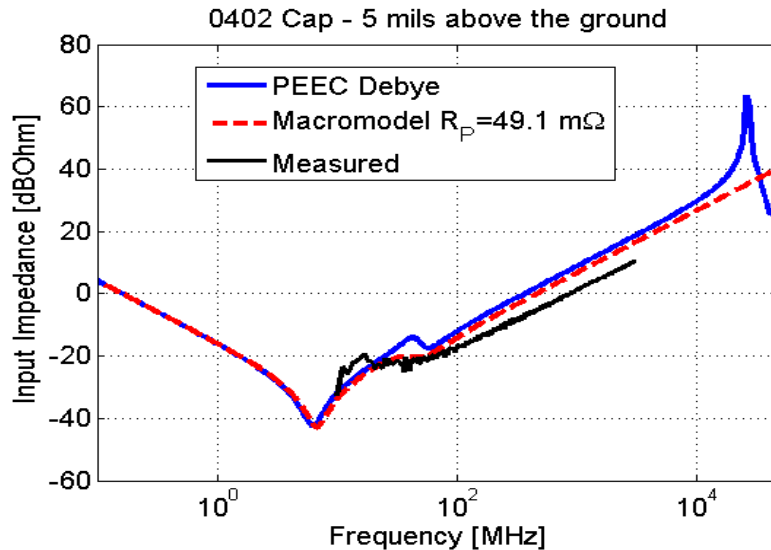


Figure 3.11. Impedance curve comparison for PEEC and macromodel

The table shown in Figure 3.12 only works for the 0402 package geometry and the 0603, 0805 package will be included in the future. Finally a library of the all the package size will be created, as long as the pad lay-out is fixed. We can choose the value from this library for responding geometry. For example, for hundreds of decoupling capacitor, as long as the lay out is fixed, we can put this simple model on top and just need to calculated the L-below.

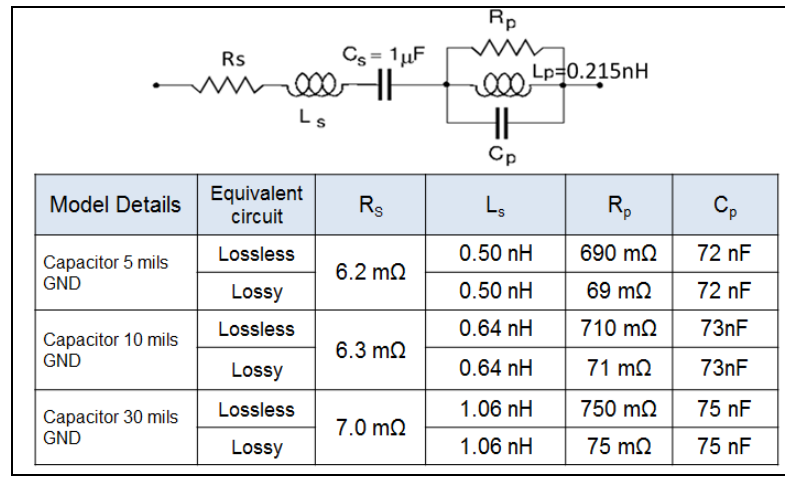


Figure 3.12. Table of equivalent circuit value for different ground spacing

4. CONCLUSIONS

The “Root-omega” method to extract the DK and DF values in a fabricated board was studied in this paper using simulations, for both cases with the smooth and rough conductors. It is found that the DK extraction works well with a relative error no more than a few percent in the entire frequency range up to 50 GHz. However, the DF extraction needs further improvement. Currently the procedure can result in a large relative error, especially for a low loss material because in general α_C is larger than α_D , which results in large errors in the curve fitting. Sensitivity analysis for DK and DF extraction was also performed to explain the observed phenomenon. Proposed new method takes advantage of differential and common mode behavior of differential stripline to remove the roughness effect and extract the transmission line based DK and DF. The extracted DK, DF and Huray factor are validated by comparing S-parameters from Intel tool simulation and measurement in different board. Good correlation between simulation and measurement can be achieved up to 20GHz in both magnitude and phase.

In section 2, we show that a good macromodel for a decoupling capacitor, which includes a local connection arrangement, provides a good solution for accurate PDN models. Such a model is computationally very efficient. Alternatively, capacitor manufacturer needs to specify internal partial inductance values and detailed physical shapes for the couplings to the capacitors such that more accurate models like the PEEC model given in this paper can be built. Aspects for future work have been exposed, like macromodels which include the distance to the ground plane and the variability due to the exact placement of the decoupling capacitor on the local connection pads.

BIBLIOGRAPHY

- [1] M Y. Koledintseva, A. Koul, S. Hinaga, and James L. Drewniak. "Differential and extrapolation techniques for extracting dielectric loss of printed circuit board laminates." Microwave Symposium Digest (MTT), 2011 IEEE MTT-S International, Baltimore, MD, 2011, pp. 1-4.
- [2] L. Hua, B. Chen, Shuai Jin, M. Koledintseva, J. Lim, K. Qiu, R. Brooks, Ji Zhang, K. Shringarpure and J. Fan. "Characterization of PCB Dielectric Properties Using Two Striplines on the Same Board." Electromagnetic Compatibility, 2014 IEEE International Symposium on, Raleigh, NC, 4-8 Aug. 2014, pp. 809 – 814.
- [3] A. Koul, P. K. R Anmula, M. Y. Koledintseva, J. L. Drewniak, and S. Hinaga. "Improved technique for extracting parameters of low-loss dielectrics on printed circuit boards." Proc. IEEE Symp. Electromag. Compat., Aug. 17-21, Austin, TX, 2009, pp. 191-196..
- [4] E. Bogatin, S. Begley, and M. Resso, "The role of dielectric constant and dissipation factor measurements in multi-gigabit systems", DesignCon, 2007, San Jose, CA, Feb. 2007.
- [5] Shuai. Jin, Ji Zhang, Jun Fan. "Optimization of transition from connector to PCB board." Electromagnetic Compatibility, 2013 IEEE International Symposium on, pp. 192 – 196
- [6] J, Lim, Kai Soon Chow, Ji Zhang, Jianmin Zhang, K. Qiu, R. Brooks, "ASIC package design optimization for 10 Gbps and above backplane serdes links." 2012 IEEE International Symposium on Electromagnetic Compatibility (EMC), vol., no., pp.199,204, 6-10 Aug. 2012
- [7] J, Lim, Ji Zhang, Wei Yao, K. Tseng, K. Qiu, R. Brooks, Jun Fan, "ASIC package to board BGA discontinuity characterization in >10Gbps SerDes links." IEEE International Symposium on Electromagnetic Compatibility, vol., no., pp.569,574, 5-9 Aug. 2013
- [8] A. Koul, M. Y. Koledintseva, S. Hinaga, and J. L. Drewniak. "Differential extrapolation method for separating dielectric and rough conductor losses in printed circuit boards." Electromagnetic Compatibility, IEEE Transactions, vol. 54, no. 2, pp. 421-433, 2012.
- [9] J R. Miller, G. Blando, and I. Novak. "Additional trace losses due to glass-weave periodic loading." Proceedings of DesignCon, pp. 1-4. 2010.

- [10] M. Y. Koledintseva, A. Razmadze, A. Gafarov, S. De, S. Hinaga, and J.L. Drewniak, "PCB conductor surface roughness as a layer with effective material parameters", IEEE Symp. Electromag. Compat., Pittsburg, PA, 2012, pp. 138-142..
- [11] M.Y. Koledintseva, J. Drewniak, S. Hinaga, F. Zhou, A. Koul, and A. Gafarov, "Experiment-based separation of conductor loss from dielectric loss in striplines", DesignCon 2011, Santa Clara, CA, Jan. 31-Feb. 3, 2011, paper 5-TP5.
- [12] A. E. Ruehli, D. Johns, and K. Shingarpure, "Partitioning systems into smaller sub-systems for EM/CKT modeling," in *Proc. of the IEEE Int. Symp. on Electromagnetic Compatibility*, Raleigh, NC, Aug. 2014
- [13] C. Wang, J. Mao, G. Selli, S. Luan, L. Zhang, J. Fan, D. J. Pommerenke, R. E. DuBroff, and J. L. Drewniak, "An efficient approach for power delivery network with closed-form expressions for parasitic interconnect inductances," *IEEE Transactions on Advanced Packaging*, vol. 29, no. 2, pp. 320–334, May 2006.
- [14] G. M. Harayda, A. Omi, and A. Yamamoto, "Improve your designs with large capacitance value multi-layer ceramic chip (mlcc) capacitors," *Panasonic, Electronic Component Brosure*, pp. 1–5, 2003.
- [15] A E. Ruehli, G. Antonini, J. Esch, J. Ekman, A. Mayo, and A. Orlandi, "Non-orthogonal PEEC formulation for time and frequency domain EM and circuit modeling." in *Proc. of the IEEE Int. Symp. on Electromagnetic Compatibility*, vol. 45, May 2003, pp. 167–176

VITA

Xiang Fang was born in Taixing, Jiangsu, China. He received his B.S. degree in Physics from Lanzhou University, Gansu, China, in 2011. He joined the EMC Laboratory in the Missouri University of Science and Technology, Rolla, in 2013 and received the M.S. degree of Electrical Engineering in December 2016. He worked as a summer Graduate Intern Engineer at DELL SI Team in 2014.

His research interests included signal integrity, power integrity, and high speed serial link design.